

Integrated rupture mechanics for slow slip events and earthquakes

Huihui Weng (✉ qfkq7850@mail.ustc.edu.cn)

UCA <https://orcid.org/0000-0002-2936-2342>

Research Article

Keywords: slow slip events, earthquakes, seismogenic zones

Posted Date: December 14th, 2021

DOI: <https://doi.org/10.21203/rs.3.rs-448196/v2>

License:  This work is licensed under a Creative Commons Attribution 4.0 International License.

[Read Full License](#)

1 Integrated rupture mechanics for slow slip events and 2 earthquakes

3 Huihui Weng^{1*}

4 ¹Université Côte d'Azur, IRD, CNRS, Observatoire de la Côte d'Azur, Géoazur, 250 rue Albert
5 Einstein, Sophia Antipolis, 06560 Valbonne, France

6 Correspondence to Huihui Weng (email: weng@geoazur.unice.fr)

7 **Slow slip events occur in subduction megathrusts and crustal faults worldwide and have the**
8 **potential to trigger devastating earthquakes. The empirical moment-duration scaling re-**
9 **lation can help constrain the physical mechanism of slow slip events, yet it is still debated**
10 **whether this scaling is linear or cubic and a fundamental model unifying slow slip events and**
11 **earthquakes is still lacking. Here I present numerical simulations that show that the rupture**
12 **propagation of slow slip events and earthquakes on long faults can be predicted by the same**
13 **three-dimensional theory of dynamic fracture mechanics. The complete spectrum of rup-**
14 **ture speeds, from arbitrarily slow speeds up to the S-wave speed, is quantitatively controlled**
15 **by the ratio of fracture energy to energy release rate, which depends on the frictional be-**
16 **haviour on the fault. I find that the heterogeneity of shear stress can produce a cubic scaling**
17 **while heterogeneity of effective normal stress produces a linear scaling, which reconciles the**
18 **debated scaling relations. This fundamental model, if combined with the lab-observed fric-**
19 **tional mechanisms, provides a new framework to explain how a slow slip event transitions**
20 **to an earthquake, and thus opens new avenues for seismic hazard assessment through the**

21 **integration of seismological, laboratory, and theoretical developments.**

22 Slow slip events (SSEs) have been observed in subduction megathrusts and crustal faults
23 worldwide¹⁻⁹, and may trigger large megathrust earthquakes¹⁰⁻¹³, therefore understanding the phys-
24 ical mechanisms of SSEs is of increasing importance. SSEs usually occur in an elongated section
25 of the deep plate interface and have rupture speeds much slower than large megathrust earthquakes,
26 whose ruptures are also elongated (Figure 1a). A compilation of rupture speeds of global SSEs¹⁴⁻¹⁶,
27 earthquakes¹⁷⁻²¹, and laboratory experiments²² illustrates that spontaneous ruptures span a wide
28 range of speeds, from ultra-slow speeds up to the P-wave speed (Figure 1b). Previous simulations
29 show that SSE ruptures can propagate steadily at a very slow speed if facilitated by a frictional
30 transition from rate-weakening at low slip rates to rate-strengthening at high slip rates²³⁻²⁵ or by
31 fault gouge dilatancy with an associated change in fluid pressure²⁶⁻²⁹, both of which are observed
32 experimentally²⁹⁻⁴⁰. In addition, earthquake ruptures on long faults can steadily propagate at super-
33 shear speeds (faster than the S-wave speed), depending on the balance between fracture energy and
34 energy release rate⁴¹. Though laboratory experiments^{22,33} and the one-dimensional (1D) continu-
35 ous Burridge-Knopoff model⁴² have suggested a continuum of rupture speeds, the general rupture
36 mechanics that controls the rupture propagation of both SSEs and earthquakes on long faults is
37 not completely understood. Empirical moment-duration scaling relations^{14,43-50} have been used
38 to compare the physical mechanisms of SSEs and earthquakes, yet it is still debated whether the
39 scaling of SSEs is linear^{43,44} or cubic^{14,45,46} and a fundamental model that integrates SSEs and
40 earthquakes is still lacking. Here, I show that the rupture propagation of SSEs and earthquakes on
41 long faults can be predicted by the same theoretical equation of motion of the rupture tip and the
42 debated scaling behaviours of SSEs can be attributed to different types of fault heterogeneities.

Previous numerical and theoretical studies^{51,52} demonstrated that dynamic rupture propagation on long faults with finite width in a 3D elastic medium is independent of the rupture length and the theoretical equation of motion of the rupture tip is expressed as (Methods A2):

$$F\left(\frac{G_c}{G_0}\right) = M(v_r) \cdot \dot{v}_r, \quad (1)$$

where G_c/G_0 is the ratio between the fracture energy and the energy release rate of steady-state ruptures, \dot{v}_r is the rupture acceleration, the time derivative of rupture speed v_r , and F and M are known universal functions⁵¹ derived from the theory of dynamic fracture mechanics of long ruptures (ruptures much longer than they are wide). Both G_c and G_0 are functions of rupture speed v_r and depend on the friction behaviour of the fault⁵³. In particular, substituting $\dot{v}_r = 0$ into equation (1) yields the energy balance condition for a steady-state rupture: $G_c(v_r) = G_0(v_r)$. Weng and Ampuero⁵¹ proposed that steady-state ruptures can propagate at any speed up to the S-wave speed if the fracture energy increases with increasing rupture speed. Further linear stability analysis (Methods A2) shows that the general stability condition for steady-state ruptures can be written as

$$\frac{d(G_c/G_0)}{dv_r} > 0. \quad (2)$$

44 Note that the opposite condition, $d(G_c/G_0)/dv_r \leq 0$, predicts that ruptures either accelerate
 45 ($G_c/G_0 < 1$) or decelerate ($G_c/G_0 > 1$), which has been numerically validated for earthquake
 46 rupture speeds⁵¹ (close to S-wave speed).

48 Here, I further validate equation (1) for a continuum of rupture speeds from arbitrarily-slow
 49 speeds up to the S-wave speed (Figure S1A) in numerical simulations controlled by a rate-and-
 50 state friction law with rate-weakening behaviour at low slip rates and rate-strengthening behaviour
 51 at high slip rates (Methods A3), as observed in laboratory experiments^{30–40}. The numerical sim-
 52 ulations show that the steady rupture speed (v_r/v_s) can be controlled by two parameters (Figure
 53 2a): the stress drop ($\Delta\tau/\sigma$) and the critical slip rate ($V_c\mu/\sigma v_s$) above which the fault friction tran-
 54 sitions from rate-weakening to rate-strengthening. Here, the quantities are nondimensionalized
 55 by the S-wave speed (v_s), effective normal stress (σ), and shear modulus (μ) (ref⁵⁴). The rupture
 56 speed increases monotonically with the stress drop and critical slip rate. Tuning these two nondi-
 57 mensional parameters can produce rupture propagation at a continuum of steady rupture speeds,
 58 including speeds of ultra-slow SSEs ($\ll v_s$), tsunami earthquakes^{17–19} ($> \frac{1}{3}v_s$), and fast subshear
 59 earthquakes ($> 0.5v_s$). In all the simulated steady models, G_c agrees with G_0 within 3% (Figure
 60 S2a), which validates equation (1). In addition, G_c increases with v_r while G_0 is a prescribed pa-
 61 rameter independent of v_r (Figure S2b & Methods A5), which satisfies the stability condition of
 62 steady-state ruptures (equation 2).

63 The numerical simulations further show that the dependence of steady rupture speed on stress
 64 drop is highly consistent for various values of critical slip rate, except for the fast subshear rup-
 65 tures (Figure S1b). The fast subshear ruptures deviate from the general trend of the slow rup-
 66 tures because of dynamic-wave effects. The effects of dynamic waves on rupture propagation have
 67 been theoretically investigated⁵¹ and characterised by a nondimensional Lorentz contraction factor,
 68 $\alpha_s = \sqrt{1 - (v_r/v_s)^2}$, a well-known function in earthquake dynamics⁵⁵. In addition, fracture me-

69 chanics theory shows that the analytical solutions of steady-state ruptures depend on $v_r/\alpha_s v_s$ rather
70 than v_r/v_s (Method A6). Therefore, the effects of dynamic waves are trivial when $v_r/v_s < 0.5$
71 (that is $v_r/\alpha_s v_s \approx v_r/v_s$), a speed range including SSEs and tsunami earthquakes, and become
72 significant as v_r approaches v_s (that is $v_r/\alpha_s v_s \rightarrow \infty$). Accounting for the Lorentz factor, I find all
73 values of steady rupture speeds, after normalization by the critical slip rate, collapse onto a univer-
74 sal curve (Figure 2b), which is predicted by the 3D theory of dynamic fracture mechanics of long
75 ruptures (Methods A5 & A6). All values of peak slip rate also collapse onto the theoretical curve
76 (Figure 2c). The consistency of these parameters with theory show that the propagation of steady
77 ruptures, for the complete spectrum of rupture speeds from arbitrarily slow up to the S-wave speed,
78 can be predicted by the same fundamental equation of motion (equation 1). The validations of the
79 steady SSE ruptures in this paper and the non-steady earthquake ruptures in a previous paper by
80 Weng and Ampuero⁵¹ prove that equation (1) can be used to describe both SSEs and earthquakes
81 in a same theoretical framework, provided the dependence of the energy ratio, G_c/G_0 , on rupture
82 speed, v_r , is known (Methods A5).

83 G_c/G_0 is controlled by the specific frictional behaviour of the fault⁵³. Because the slip rate
84 and rupture speed are positively correlated (Methods A6), rate-and-state friction law with rate-
85 strengthening at high slip rates, as observed in laboratory experiments³⁰⁻⁴⁰, produces a V-shaped
86 G_c/G_0 as a function of v_r that decreases at low v_r and increases at high v_r (Figure S2d). Other fric-
87 tional mechanisms, such as fault gouge dilatancy with an associated change in fluid pressure²⁶⁻²⁹,
88 also induce frictional strengthening at high slip rates and may produce a V-shaped G_c/G_0 . More-
89 over, fault friction may dramatically decrease at higher seismic slip rates (e.g., $> 0.1m/s$) con-

90 trolled by flash heating^{35–37,56} and thermal pressurization^{56,57}. Flash heating, dominant at small
91 earthquake slips, is a rate-weakening mechanism and thus is expected to produce a decreasing
92 G_c/G_0 as a function of v_r . At larger slips, the weakening controlled by thermal pressurization or by
93 off-fault inelasticity (bulk plasticity or damage) is slip-dependent rather than rate-dependent^{56–58},
94 and thus G_c/G_0 is a function⁴¹ of the final slip (D) independent of v_r , $G_c/G_0 \propto D^{n-2}$, where
95 $n = 2/3$ for thermal pressurization⁵⁷ and $n = 1$ for theoretical off-fault inelastic dissipation⁵⁸.
96 Therefore, considering that D is bounded by the interseismic slip deficit, the larger the accu-
97 mulated slip deficit on the fault, the smaller G_c/G_0 can be. Combining the above mechanisms
98 dominant at different slip rates and slips, I propose a conceptual model for G_c/G_0 (Figure 1c) that
99 provides an explanation for the seismological observations^{10–13} that show that SSEs may trigger
100 large earthquakes in their adjacent areas. Assuming a rupture starts in a low-coupling fault seg-
101 ment where the rate-strengthening mechanism dominates (due to insufficient slip deficit; purple
102 curve in Figure 1c), the rupture speed is confined to a low and stable value and thus only forms an
103 SSE. If this SSE propagates into the adjacent fault segment where the thermal weakening mech-
104 anism dominates (due to sufficient slip deficit; red curves in Figure 1c), this steady SSE could
105 transition to a non-steady earthquake and accelerate toward the S-wave speed, which is consistent
106 with the 2D cycle simulations with gauge dilatancy and thermal pressurization⁵⁹. Note that there
107 may be two admissible steady speeds if the two competing frictional mechanisms are comparable
108 (dash red curve in Figure 1c); but I propose that the rupture is more likely to accelerate toward the
109 S-wave speed, which remains to be confirmed in numerical simulations. While the G_c/G_0 model
110 presented here is qualitative, it serves as an example of how SSEs and earthquakes can be investi-

111 gated within the same theoretical framework that combines fracture mechanics theory, laboratory,
112 and seismological observations.

113 **Along-strike rupture segmentation**

114 Additional results of simulations of non-steady ruptures due to fault heterogeneities demonstrate
115 that non-steady SSEs can also be described by the same theoretical equation of motion. When a
116 steady rupture propagates into a segment of higher shear stress, the rupture jumps from one steady
117 state to another via a transient (Figure 3a). The rupture speed transients of quasi-dynamic SSEs
118 are very similar to those of dynamic ruptures of $v_r/v_s < 0.5$, while the transition distances of fast
119 ruptures (close to S-wave speed) are quantitatively longer due to the dynamic-wave effects. On the
120 other hand, if the shear stress of the segment is lower than the minimum for steady ruptures, the
121 segment behaves as a barrier so the rupture decelerates and finally arrests after penetrating a certain
122 distance (Figure 3b). In general, the arresting distance increases with the peak slip rate attained
123 before the rupture reached the barrier, while the arresting distances of fast ruptures are longer due
124 to the dynamic-wave effects.

125 The reason that fast ruptures have longer transition and arresting distances than slow ruptures
126 can be understood by the 3D theory of dynamic fracture mechanics of long ruptures (equation 1).
127 The apparent mass, $M(v_r/v_s)$, in the equation of motion is nearly constant when $v_r/v_s < 0.5$
128 and increases to infinity as v_r approaches v_s (Methods A2). This is similar to the relativistic mass
129 in Einstein's theory of relativity, which contains the same Lorentz factor with the S-wave speed

130 replaced by the speed of light. Because of this "inertial" effect, a larger mass, $M(v_r/v_s)$, due to a
131 high rupture speed ($v_r \rightarrow v_s$) makes such ruptures harder to stop within a barrier or to transition to
132 another steady state, which therefore explains why the fast ruptures require longer transition and
133 arresting distances.

134 Geophysical observations^{8,14,60} show that SSEs usually rupture each segment downdip of the
135 seismogenic zone separately, but some SSEs can occasionally bridge multiple segments and reach
136 larger magnitudes, which conceptually resembles the supercycle behaviour of large megathrust
137 earthquakes occurring in seismogenic zones^{61,62}. This supercycle-like behaviour of SSEs can be
138 explained by the time-dependent evolution of SSE segmentation. Both the numerical simulations
139 and theory demonstrate that there is a critical stress drop for steady SSEs (Figure 2b & Method
140 A7), which is $\Delta\tau^{steady}/\sigma \approx 0.01$, given the rate-and-state frictional parameters used in this paper,
141 where σ is the effective normal stress. On dip-slip faults, a critical final slip is approximately
142 related to the critical stress drop⁴¹ by $D^{steady} = 2W\Delta\tau^{steady}/\pi\mu$, where W is the SSE fault width
143 and μ is the shear modulus. SSE fault segments need to accumulate sufficient slip deficit, that is
144 $D^{steady} = 0.02W\sigma/\pi\mu$, to be capable of accommodating steady SSE ruptures, otherwise they act
145 as barriers to stop rupture propagation. Therefore the recurrence interval of steady ruptures can
146 be estimated by the ratio of D^{steady} to the slip deficit rate on the fault segments during the inter-
147 SSE period. The observed slip deficit rates on SSE fault segments in subduction zones globally
148 are diverse, ranging from $< 10\%$ up to $> 50\%$ of the plate convergence rate^{8,63-65}, which can
149 be explained by different values of fault properties in cycle simulations⁶⁶. As rough lower bound
150 estimates, values of $\sigma \sim 0.1 - 1$ MPa, $W \sim 40$ km, $\mu \sim 40$ GPa, and 100% coupling at a

151 plate convergence rate of $10^{-9} m/s$ yield $\Delta\tau^{steady} \sim 0.001 - 0.01 MPa$ and recurrence times of
 152 $\sim 0.2 - 2$ months, which are comparable to the typical stress drops of $0.001 - 0.2 MPa$ ^{14,44,67} and
 153 typical recurrence times of months to years^{8,68} of SSEs globally.

154 The recurrence intervals of large megathrust earthquakes⁶² are much longer than those of
 155 SSEs. Laboratory experiments⁶⁹ and theoretical models^{56,57} of thermal weakening show that
 156 rock friction exponentially decays from a peak to a residual value, resulting in an upper bound
 157 estimate⁶⁹ of fracture energy: $G_c \approx A(\mu_p - \mu_r)\sigma^{1-B}$, where μ_p and μ_r are the peak and resid-
 158 ual friction coefficients, respectively, and the coefficients A and B can be experimentally deter-
 159 mined. The energy release rate on a long fault is $G_0 = \Delta\tau^2 W / \pi\mu$ (Methods A5), therefore the
 160 critical stress drop for runaway earthquake ruptures, derived from the condition $G_c/G_0 < 1$, is
 161 $\Delta\tau^2/\sigma^{1-B} \approx A\pi(\mu_p - \mu_r)\mu/W$. Given $A \approx 3 - 78$, $B \approx 1.18$, and $\mu_p - \mu_r \approx 0.7$ in laboratory
 162 experiments(ref⁶⁹), and $W \sim 40 km$ and $\mu \sim 40 GPa$, we have $\Delta\tau^{run} \approx 2.6\sigma^{-0.09} - 13\sigma^{-0.09}$,
 163 which is insensitive to σ because the exponential coefficient is close to zero. Note that $\Delta\tau^{run}$ is
 164 an upper bound estimate here. For $\sigma > 20MPa$, $\Delta\tau^{run} \approx 2 - 10MPa$ is comparable to the
 165 average stress drop of $\sim 4MPa$ of global large earthquakes⁷⁰. Assuming the stress drop of large
 166 earthquakes is close to $\Delta\tau^{run}$ (runaway occurs at the first possible moment), the fault strength
 167 during the interseismic period increases from the residual value $\sigma\mu_r$ to $\sigma\mu_r + \Delta\tau^{run}$, resulting in
 168 an average apparent fault strength of $\sigma\mu_r + 0.5\Delta\tau^{run}$ given a constant stressing rate. The appar-
 169 ent fault strength is much smaller than the static fault strength of earthquake ruptures ($\sigma\mu_p$) when
 170 $\sigma > 50MPa$, that is $\mu_r + 0.5\Delta\tau^{run}/\sigma \ll \mu_p$, which can explain why some crustal faults are much
 171 weaker than the predicted static fault strength⁷¹. As a rough lower bound estimate of the recurrence

172 interval, 100% coupling at a plate convergence rate of 10^{-9} m/s yields $\sim 40 - 200$ years, which
173 is comparable to the recurrence times of tens to hundreds years of large earthquakes⁶². Large
174 earthquake supercycles are challenging to study due to their long recurrence times, but the formal
175 connections between regular earthquakes and SSEs revealed here indicate that future investigations
176 of the kinematics and dynamics of frequent SSEs will enable the building of a comprehensive SSE
177 supercycle model, which in turn will help to better understand the supercycle behaviour of large
178 devastating earthquakes.

179 **Observations of SSEs and earthquakes**

180 The comparison of moment-duration scaling relations between SSEs and earthquakes has been
181 considered in discussions of their physical mechanisms^{14,43-50}, however the moment-duration rela-
182 tion of SSEs observed in a particular environment features a cubic scaling¹⁴ that is radically differ-
183 ent from the linear scaling observed in a global compilation from different fault environments⁴³.
184 Here, I show that the debated scaling behaviours can be attributed to different types of fault het-
185 erogeneities: heterogeneity of shear stress can produce a cubic scaling, whereas heterogeneity of
186 effective normal stress produces a linear scaling. The relation between moment (M_0) and dura-
187 tion (T) is $M_0 \propto \Delta\tau W^2 L$ for long ruptures⁷², where $L = v_r T$ is the rupture length and $\Delta\tau$ and
188 v_r are the stress drop and rupture speed, respectively. Defining $\Delta\tau \propto L^\alpha$ and $v_r \propto L^\beta$ leads
189 to $M_0 \propto T^{\frac{1+\alpha}{1-\beta}}$, where α and β are constant coefficients. For a homogeneous model (Methods
190 A8), ruptures with different values of uniform $\Delta\tau$ produce a linear moment-duration scaling (Fig-
191 ure 4a). However if the shear stress distribution in the fault is heterogeneous, and in particular

192 if it decays linearly away from the nucleation area (Methods A8), the simulated models result in
193 $\alpha = 0.5$ and $\beta = 0.5$, which leads to a cubic scaling relation (Figure 4a & S3), consistent with the
194 observations in a particular environment¹⁴. Although this is one specific case of heterogeneity, it
195 demonstrates that a cubic scaling relation can be produced by heterogeneity of shear stress within
196 a particular fault, as also observed in an SSE cycle model⁵⁰.

197 Moreover, such a cubic scaling curve, obtained under the assumption of constant effective
198 normal stress σ , is diagonally shifted if σ varies over a significant range, in a way that produces a
199 linear $M_0 \propto T$ envelope (Figure 4b). This is predicted by the theoretical relations $M_0 \propto \Delta\tau \propto \sigma$
200 and $T \propto 1/v_r \propto \sigma$ (Method A8), which imply $M_0 \propto T$ when only σ is varied. Therefore, when
201 mixing data with diverse values of σ , a linear envelope of the $M_0 - T$ scaling, different from that
202 of regular earthquakes, can be obtained. This can explain the observed linear scaling based on a
203 global compilation of various slow earthquakes from different fault environments whose σ may
204 span several orders of magnitude, such as $\sigma \sim 1 - 10kPa$ on the deep San Andreas fault⁷³ and
205 $\sigma > 1MPa$ in the Izu-Bonin Trench¹⁶. None of the other parameters of the model produce a linear
206 envelope when varied, which would require M_0 and T to have the same scaling dependence on
207 that parameter.

208 To explore the scaling relation of rupture speeds that can be directly compared with frac-
209 ture mechanics theory, I compiled and calculated the rupture speeds and peak slip rates of global
210 SSEs, earthquakes, and lab experiments (Figure 1b & Methods A1). In general, the observed rup-
211 ture speed increases with the observed peak slip rate, enveloped by two theoretical predictions

212 with peak-to-residual strength drops of $\Delta\tau_{p-r}/\mu = 10^{-6}$ and $\Delta\tau_{p-r}/\mu = 10^{-4}$ at the rupture tip
 213 (Figure 1b). Assuming the stress drops of SSEs are approximately the minimum value of steady
 214 ruptures, as suggested based on cycle simulations²³, the effective normal stress of the SSEs can
 215 be constrained by the theoretical relation, $\sigma \approx \Delta\tau_{p-r}/0.07$ (Methods A7). Given $\mu = 40GPa$,
 216 the constrained σ of the SSEs and lab experiments lies between $\sim 0.6 - 60MPa$. In addition,
 217 another theoretical relation, $V_c/\sigma \approx v_r^{steady}/50\mu$ (Methods A7), can constrain the critical slip rate:
 218 $V_c \sim 3 \times 10^{-9} - 3 \times 10^{-4}m/s$, which is consistent with the reported values, that is $10^{-9} - 10^{-2}m/s$,
 219 in laboratory experiments³⁴⁻⁴⁰. Note that the uncertainty for constraining V_c alone is larger than
 220 that for the ratio V_c/σ , because the former requires estimates of both rupture speed and peak slip
 221 rate and the latter only requires estimates of rupture speed.

222 Although a continuum of rupture speeds has been reported in laboratory experiments^{22,33},
 223 there exists an observation gap of rupture speeds in natural faults between $10 - 1000m/s$ (Figure
 224 1b). The numerical models show that a continuum of rupture speeds can be obtained by tuning
 225 two nondimensional parameters, $\Delta\tau/\sigma$ and $V_c\mu/\sigma v_s$ (Figure 2a). In the opposite case, a gap of
 226 rupture speeds is expected if $\Delta\tau/\sigma$ and $V_c\mu/\sigma v_s$ are not diverse. The SSE cycle simulations²³
 227 showed that $\Delta\tau/\sigma$ of SSEs is close to the minimum value of steady ruptures $\Delta\tau^{steady}/\sigma$, and thus
 228 it is reasonable to assume that rupture speed is mainly controlled by $V_c\mu/\sigma v_s$, that is $v_r/v_s \approx$
 229 $50V_c\mu/\sigma v_s$ (Methods A7). Here, I propose two explanations for the gap of rupture speeds in
 230 natural faults. The first one is that the maximum $V_c\mu/\sigma v_s$ in natural faults is much smaller than the
 231 maximum value reported in laboratory experiments on natural and synthetic fault gouges (Figure
 232 2d). If $V_c\mu/\sigma v_s < 10^{-4}$ in natural faults then G_c/G_0 is expected to be an increasing function of

233 v_r for $v_r < 10m/s$ and a decreasing function for $v_r > 10m/s$, where the former produces steady
234 SSEs with $v_r < 10m/s$ (gray area in Figure 1c) and the latter produces non-steady earthquakes
235 with an average rupture speed of $v_r > 1000m/s$ (pink area in Figure 1c). The second explanation
236 is that values of $V_c\mu/\sigma v_s > 10^{-4}$ are possible in natural faults (gray area overlaps with pink area in
237 Figure 1c), but are very rare so that we have not yet observed events within the intermediate speed
238 range. This explanation can be justified by observations in laboratory experiments²² that show
239 that events with rupture speeds between $10 - 1000m/s$ are rarer than slower ruptures. However,
240 more work is needed either to explain why $V_c\mu/\sigma v_s$ in natural faults is not as diverse as observed
241 in laboratory experiments or to fill the observational gap of rupture speeds in natural faults, by
242 capitalizing on advances in rock mechanics, geodesy and seismology.

243 Earthquake ruptures on long faults can steadily propagate at speeds of $> \frac{1}{3}v_s$ if $V_c\mu/\sigma v_s >$
244 6×10^{-3} , which provides a possible new mechanism to explain the anomalously slow tsunami
245 earthquakes^{17-19,74}. Given $\sigma = 20 MPa$, $\mu = 40GPa$, and $v_s = 3330m/s$, values of V_c are
246 required to be larger than $10^{-2} m/s$, which is the upper bound of the observed values in laboratory
247 experiments³⁴⁻⁴⁰. As the frictional strength may change from rate-strengthening to rate-weakening
248 at slip rates higher than $0.1 m/s$ due to the thermal weakening mechanisms that facilitate fast
249 earthquakes³⁵⁻³⁷, the narrow range of rate-strengthening behaviour between $10^{-2} m/s$ and $0.1 m/s$
250 may explain the scarcity of tsunami earthquakes. Alternative explanations for tsunami earthquakes
251 are low rigidity materials⁷⁵ and inelastic material within and/or around the fault⁷⁶, and the density
252 and size of asperities⁷⁷, which remain to be confirmed by further investigations.

253 While the rock frictional behaviour may be controlled by different mechanisms, the rupture
254 propagation of both slow and fast events on long faults can be predicted by the same 3D theory of
255 dynamic fracture mechanics and the rupture speed is quantitatively controlled by G_c/G_0 . Integrat-
256 ing laboratory and theoretical developments of frictional mechanisms in quantifying G_c/G_0 , this
257 basic model would enable a quantitative description of both the short-term slow ruptures and the
258 long-term supercycle behaviours associated with devastating earthquakes within the same theoret-
259 ical framework. This fundamental model integrates slow and fast ruptures, reconciles the debated
260 scaling relations, and thus opens new avenues for assessing the future seismic hazard through
261 integration of observations and models of frequently occurring SSEs and devastating earthquakes.

262 **Methods**

263 **A1. Estimates of rupture speed and peak slip rate** To explore a universal scaling relation in
264 global SSEs, earthquakes, and lab experiments, I compiled different datasets from the literature^{14,16–19,22}
265 and online databases^{15,20,21} and calculated their rupture speed and peak slip rate. For SSEs and
266 earthquakes, the rupture speed is estimated by $v_r = L/T$, with an uncertainty of a factor of 2 for
267 bilateral ruptures, where L and T are the rupture length and duration, respectively. The peak slip
268 rate is estimated by $V_p = \gamma D/\tau_{rise}$, where D is the average slip, τ_{rise} is the rise time, and γ is
269 an empirical ratio that links the peak and average slip rates. For ruptures with aspect ratios ≥ 1 ,
270 the rise time is approximately estimated by $\tau_{rise} = TW/L$, where W is the rupture width. L , W ,
271 D , and T of SSEs are constrained by geodetic observations^{14–16}. L , W , and D of earthquakes are
272 constrained by finite-fault rupture models^{17–20}; T of three tsunami earthquakes is constrained by
273 finite-fault rupture models^{17–19} and T of other earthquakes is constrained by independent source
274 time functions²¹. $\gamma \approx 20$ is assumed for both SSEs and earthquakes based on the results of nu-
275 merical simulations (Figure S4). Note that the uncertainty of γ affects the values of peak slip
276 rate, whereas it does not affect the values of rupture speeds. The rupture speed in laboratory
277 experiments²² is directly measured by the strain gage array and the peak slip rate is estimated from
278 the direct measurements of the dynamic stress drop and rupture speed.

A2. General conditions for steady ruptures on long faults For subshear mode III (dip-slip),
rupture propagation on long faults with finite width (W) in a 3D elastic medium can be predicted

by a theoretical rupture-tip equation of motion⁵¹

$$F(G_c/G_0) = M(v_r) \cdot \dot{v}_r, \quad (3)$$

where

$$F(G_c/G_0) = 1 - G_c/G_0, \quad (4)$$

$$M(v_r) = \frac{W}{v_s^2} \frac{\gamma}{A\alpha_s^P},$$

G_c and G_0 are the fracture energy and energy release rate, v_r is the rupture speed, \dot{v}_r is the rupture acceleration, v_s is the S-wave speed, $\alpha_s = \sqrt{1 - (v_r/v_s)^2}$ is the Lorentz contraction factor, and γ , A , and P are known coefficients⁵¹. In general, this equation of motion can be expressed as

$$F\left(\frac{G_c(v_r)}{G_0(v_r)}\right) = M(v_r) \cdot \dot{v}_r, \quad (5)$$

279 where $G_0(v_r)$ and $G_c(v_r)$ are a function of v_r that depends on the specific friction law⁵³.

For steady-state ruptures, $\dot{v}_r = 0$, thus the first condition for steady ruptures is

$$G_c(v_r) = G_0(v_r). \quad (6)$$

For the stability analysis, I define

$$f(\dot{v}_r, v_r) \equiv \frac{1 - M(v_r)\dot{v}_r}{G_c(v_r)/G_0(v_r)}, \quad (7)$$

where function $F()$ can be written as a linear expansion near the steady-state solution $\dot{v}_r = 0$

$$f(\dot{v}_r, v_r) \approx f(0, v_r) + \frac{\partial f(0, v_r)}{\partial \dot{v}_r} d\dot{v}_r + \frac{\partial f(0, v_r)}{\partial v_r} dv_r = 1. \quad (8)$$

Suppose a positive perturbation of v_r is applied to the steady-state rupture tip, that is $dv_r > 0$, the rupture can be stable only when the response of \dot{v}_r is negative, that is $d\dot{v}_r < 0$. Therefore the

stability condition for a steady solution is

$$\frac{\partial f}{\partial \dot{v}_r} \cdot \frac{\partial f}{\partial v_r} > 0. \quad (9)$$

Because $\partial f / \partial \dot{v}_r \propto -M(v_r) < 0$, thus a steady-state rupture requires

$$\frac{\partial f(0, v_r)}{\partial v_r} < 0. \quad (10)$$

Since $G_c(v_r) > 0$ and $G_0(v_r) > 0$, we have

$$\frac{d(G_c/G_0)}{dv_r} > 0. \quad (11)$$

Considering $F(0, v_r) = 1$, equation 11 yields

$$\frac{dG_c(v_r)}{dv_r} > \frac{dG_0(v_r)}{dv_r}. \quad (12)$$

280 **A3. Quasi-dynamic SSE rupture simulations** I consider a 3D dip-slip rupture problem on an
 281 infinitely long fault with finite seismogenic width, W , embedded in a full-space, linear elastic, ho-
 282 mogeneous medium. This 3D elongated rupture problem has been successfully approximated by
 283 a reduced-dimensionality (2.5D) model, which accounts for the elongated features while having a
 284 low computational cost^{23,51}. To facilitate a comprehensive comparison between numerical simula-
 285 tions and fracture mechanics theory, I investigate the rupture propagation of SSEs and earthquakes
 286 using 2.5D single-rupture simulations with prescribed initial conditions. The simulations of SSEs
 287 are quasi-dynamic, while the simulations of earthquakes are fully dynamic, as explained in Meth-
 288 ods A4. The shear modulus and S-wave speed of the medium are denoted μ and v_s , respectively.

The frictional strength, τ , of faults is controlled by a rate-and-state friction law with rate-weakening behaviour at low slip rates and rate-strengthening behaviour at high slip rates⁷⁸, which has been used to investigate the rupture propagation of SSEs^{23–25,79}

$$\tau = f^* \sigma + a \sigma \ln \left(\frac{V}{V^*} \right) + b \sigma \ln \left(\frac{V_c \theta}{D_c} + 1 \right), \quad (13)$$

where σ is the effective normal stress, f^* and V^* are arbitrary reference values, D_c is the characteristic slip distance, a and b are nondimensional parameters, V is the slip rate, θ is the state, and V_c is a critical slip rate. Rock exhibits rate-weakening frictional behaviour when $a - b < 0$, and the critical slip rate V_c controls the transition from rate-weakening to rate-strengthening²³. The evolution of state θ is described by the aging law⁸⁰

$$\dot{\theta} = 1 - \frac{V\theta}{D_c}, \quad (14)$$

289 where $\dot{\theta}$ is the time derivative of θ .

For each single-rupture model, one of the primary parameters that affects the rupture propagation is the initial shear stress τ_i , which equals the frictional strength and is prescribed by the values of initial slip rate V_i and state θ_i

$$\tau_i = f^* \sigma + a \sigma \ln \left(\frac{V_i}{V^*} \right) + b \sigma \ln \left(\frac{V_c \theta_i}{D_c} + 1 \right), \quad (15)$$

The nondimensional parameters, a/b and W/L_c , also affect the rupture propagation²³, where

$$L_c = \frac{\mu D_c}{b \sigma}. \quad (16)$$

290 In this study, I fix the nondimensional ratios of $a/b = 0.8$ and $W/L_c = 400$, and systematically
291 vary τ_i and V_c . The specific values of the frictional parameters are prescribed as: $\sigma = 20 \text{ MPa}$, $b =$

292 0.015, $W = 40 \text{ km}$, $D_c = 10^{-3} \text{ m}$, $f^* = 0.6$, and $V^* = 10^{-9} \text{ m/s}$; although the choice of these
293 values does not affect the conclusion of this paper, because both the computational and analytical
294 results are presented in nondimensional form. To facilitate the comparison with fracture mechanics
295 theory, the loading due to the plate convergence during rupture propagation is not considered and
296 the systematically varied τ_i in this study represents different interseismic or inter-SSE phases.

297 A nucleation zone of length $0.5W$ with higher slip rates ($\geq 10V_c$), which slowly loads its
298 surrounding region, is prescribed to smoothly nucleate unilateral ruptures. Outside the nucleation
299 zone rupture propagation is spontaneous. A stronger nucleation, such as the overstressed nucle-
300 ation condition, results in slight oscillations of rupture speed in the fully dynamic rupture models,
301 but does not affect the steady rupture speed (Figure S5). I use the boundary element software
302 QDYN⁸¹ for the quasi-dynamic SSE simulation, where the fault is infinitely long and the fault slip
303 is horizontally periodic with a prescribed length, $11W$. To avoid the interaction of the periodic
304 fault segments, a buffering segment of length $5.5W$ is set, where the frictional behaviour is rate-
305 strengthening with $a > b$. Sufficient numerical resolution is guaranteed by setting a small grid size
306 (Δx), that is, $L_c/\Delta x = 8$. The simulated time is set long enough to capture the whole rupture
307 propagation. For each single-rupture model, the rupture time on each node of the faults is deter-
308 mined by a criterion of slip rate, $10V_i$, and the rupture speed is computed based on the along-strike
309 gradient of the rupture time.

310 **A4. Fully dynamic earthquake rupture simulations** The 2.5D single-rupture simulations for
311 earthquakes are fully dynamic, conducted by a spectral element software SEM2DPACK⁸². For a
312 quantitative comparison between SSE and earthquake simulations, the same friction law and pa-

313 rameters are assumed in the dynamic earthquake rupture simulations, except for larger values of
 314 V_c , and the additional thermal weakening^{56,83} at slip rate $> 0.1 \text{ m/s}$ is not considered. Previous
 315 theoretical studies⁵¹ have suggested that the additional thermal weakening can affect the rupture
 316 speeds via controlling the dissipated⁵⁷ and potential⁸³ energies on faults, which remains to be quan-
 317 titatively investigated in the future. For simulations with rupture speeds close to the S-wave speed,
 318 a sufficiently large computational domain is set to avoid the effects of the reflected waves from
 319 the domain boundaries within the simulated time. For simulations with slow rupture speeds, the
 320 seismic radiation is relatively weak and can be well absorbed by the default absorbing boundaries
 321 in SEM2DPACK, and therefore, the simulated times are allowed to be several times longer than
 322 those for fast rupture speeds. The time step is set based on the Courant-Friedrichs-Lewy stability
 323 condition, and the grid size is the same as the quasi-dynamic SSE simulation, that is $L_c/\Delta x = 8$.

A5. Energy balance of steady SSEs and earthquakes For SSE and earthquake ruptures on long
 faults with finite width W , the energy release rate and dissipated fracture energy can be derived
 in the theoretical framework of 3D dynamic fracture mechanics. The energy release rate G_0 is the
 rate of mechanical energy flow into the rupture tip per unit rupture advance, which is dissipated by
 the fracture energy G_c for steady ruptures. For dip-slip faulting, the energy release rate G_0 depends
 on the static stress drop ($\Delta\tau$) and fault width:

$$G_0 = \frac{\lambda\Delta\tau^2W}{\mu}, \quad (17)$$

where λ is a geometrical factor, with $\lambda = 1/\pi$ for a deep buried fault⁵¹. The fracture energy G_c depends on the strength evolution on the fault⁸⁴:

$$G_c = \int_0^D [\tau(\delta) - \tau(D)] \cdot d\delta, \quad (18)$$

324 where $\tau(\delta)$ is the fault strength as a function of fault slip, δ , and D is the final slip. Equations 17
 325 and 18 are the generic definitions of energies of ruptures on long faults, regardless of the specific
 326 friction law. Below, I propose an approach to estimate G_0 and G_c under the framework of the
 327 V-shape rate-and-state friction law explained in Methods A3.

G_0 is a function of the static stress drop, the difference of shear stress before and after the ruptures

$$\Delta\tau = \tau_i - \tau_f, \quad (19)$$

where τ_i are τ_f are the initial shear stress and final shear stress, respectively. The rupture simulations of V-shape rate-and-state friction²³ have shown that the fault strength approximately drops to the minimum steady-state strength and stays there until the end of the ruptures, which is a feature different from the regular rate-and-state friction law with aging law⁸⁵. The minimum steady-state strength²³ is

$$\tau_f = f^* \sigma + a\sigma \ln \left(\frac{b-a}{a} \frac{V_c}{V^*} \right) + b\sigma \ln \left(\frac{a}{b-a} + 1 \right). \quad (20)$$

Combining equations 15 and 19 with 20 yields the close-form static stress drop

$$\Delta\tau = a\sigma \ln \frac{aV_i}{(b-a)V_c} + b\sigma \ln \frac{\frac{V_c\theta_i}{D_c} + 1}{\frac{a}{b-a} + 1}. \quad (21)$$

Equation 21 predicts the numerical values of $\Delta\tau$ well in all the simulated steady models (Figure

S2c). Substituting equation 21 into equation 17 yields the theoretical energy release rate

$$G_0 = \frac{\lambda b^2 \sigma^2 W}{\mu} \cdot \left[\frac{a}{b} \ln \frac{a V_i}{(b-a) V_c} + \ln \frac{\frac{V_c \theta_i}{D_c} + 1}{\frac{a}{b-a} + 1} \right]^2. \quad (22)$$

328 The main feature in equation 22 is that G_0 only depends on the prescribed parameters and is
 329 independent of the peak slip rate V_p . As only τ_i and V_c are systematically investigated in this study,
 330 G_0 can be written as $G_0(\tau_i, V_c)$.

G_c is an integral function of the fault strength $\tau(\delta)$ about the slip δ . The numerical simulations show that fault strength governed by V-shape rate-and-state friction has two weakening stages: the first stage accounts for the fast weakening process within the narrow cohesive zone and the second stage accounts for the slow weakening process outside the cohesive zone (Figure S6). In the first weakening stage, the strength drop, $\Delta\tau_{p-r}$, and the critical slip-weakening distance, d_c , can be predicted well by the theoretical equations²³

$$\begin{aligned} \Delta\tau_{p-r} &= b\sigma \left[\ln \left(\frac{V_c \theta_i}{3D_c} + 1 \right) - \ln \left(\frac{3V_c}{V_p} + 1 \right) \right], \\ d_c &= D_c \left[\ln \left(\frac{V_c \theta_i}{3D_c} + 1 \right) - \ln \left(\frac{3V_c}{V_p} + 1 \right) \right], \end{aligned} \quad (23)$$

where V_p is the peak slip rate and the factor 3 is an approximation of the non-uniform slip rate within the cohesive zone, which was proposed to be 2 by Hawthorne and Rubin²³. Thus, the fracture energy within the cohesive zone is estimated as

$$G_{c1} = \frac{1}{2} d_c \Delta\tau_{p-r} = \frac{1}{2} b\sigma D_c \left[\ln \left(\frac{V_c \theta_i}{3D_c} + 1 \right) - \ln \left(\frac{3V_c}{V_p} + 1 \right) \right]^2. \quad (24)$$

The contribution of fracture energy of the second weakening stage also needs to be considered.

Here, I account for this part of the total fracture energy by

$$G_{c2} = \frac{1}{2} (d_c + D) (\tau_r - \tau_f), \quad (25)$$

where D is the final slip, $\tau_r - \tau_f$ is the overshooting stress, and τ_r is the fault strength at the tail of the cohesive zone

$$\tau_r = f^* \sigma + a\sigma \ln \left(\frac{V_p}{3V^*} \right) + b\sigma \ln \left(\frac{3V_c}{V_p} + 1 \right), \quad (26)$$

$$\tau_r - \tau_f = a\sigma \ln \left(\frac{aV_p}{3(b-a)V_c} \right) + b\sigma \ln \left(\frac{\frac{3V_c}{V_p} + 1}{\frac{a}{b-a} + 1} \right). \quad (27)$$

For ruptures on long faults with finite width W , the final slip, D , is linearly proportional to the static stress drop, $\Delta\tau$, that is⁴¹

$$D = \frac{2\lambda W}{\mu} \cdot \Delta\tau. \quad (28)$$

331 Substituting equations 21, 28, 23, and 27 into equation 25 yields the close-form function of the
 332 second part of the fracture energy, G_{c2} . Therefore, the close-form function of total fracture energy
 333 is given by $G_c = G_{c1} + G_{c2}$. As G_c depends on τ_i , V_c , and the undetermined peak slip rate V_p , it
 334 can be written as $G_c(V_p, \tau_i, V_c)$.

For steady ruptures, the energy release rate shall be balanced by the dissipated fracture energy:

$$G_c(V_p, \tau_i, V_c) = G_0(\tau_i, V_c). \quad (29)$$

Equation 29 shows that the peak slip rate, V_p , of steady ruptures can be uniquely determined from the energy balance condition of V-shape rate-and-state friction. I find that equation 29 predicts the relations among V_p , $\Delta\tau$, G_0 , and G_c well in all the simulated steady ruptures (Figure 2c & S2). Method A6 shows that the steady rupture speed, v_r , monotonically depends on V_p , thus equation 29 can also be written as:

$$G_c(v_r; \tau_i, V_c) = G_0(\tau_i, V_c). \quad (30)$$

A6. Relation between peak slip rate and rupture speed A linear relation between peak slip rate and rupture speed for steady SSEs has been proposed by Hawthorne and Rubin²³

$$V_p = \frac{v_r}{C} \cdot \frac{\Delta\tau_{p-r}}{\mu}, \quad (31)$$

335 where $C \approx 0.5 - 0.55$ is an empirical geometrical factor. But this relation does not include the
 336 effects of dynamic waves when the rupture speed approaches the S-wave speed. Alternatively,
 337 Gabriel et al⁵⁸ have provided a theoretical relation between peak slip rate and rupture speed for 2D
 338 strike-slip faulting earthquakes whose rupture speeds are close to the S-wave speed. Here, I extend
 339 their 2D strike-slip relation to a dip-slip relation for the 3D long rupture problem, which physically
 340 incorporates equation 31, as explained below.

Weng and Ampuero⁵¹ demonstrated that if the cohesive zone size on long faults is much smaller than fault width, $L_c \ll W$, then the energy release rate has the following form:

$$G_{tip} = \frac{1}{2\mu} A(v_r) K_{tip}^2, \quad (32)$$

where $A(v_r) = 1/\alpha_s$, $\alpha_s = \sqrt{1 - (v_r/v_s)^2}$ is the Lorentz contraction term and K_{tip} is the stress intensity factor. By removing the strike-slip term $1 - \nu$ and replacing $A(v_r)$ by $1/\alpha_s$ in equation (18) in Gabriel et al⁵⁸, I obtain the dip-slip relation between peak slip rate and rupture speed, similar to a classical 2D result⁸⁶

$$V_p = \frac{v_r}{\alpha_s} \cdot \frac{2\Delta\tau_{p-r}}{\mu}, \quad (33)$$

where the correction of a factor of 2 is made to fit the numerical results. If $v_r \ll v_s$, then the Lorentz term $\alpha_s = 1$, and equation 33 is the same as equation 31 proposed for SSEs by Hawthorne

and Rubin²³. Note that $\Delta\tau_{p-r}$ is a function of V_p/V_c (equation 23), and thus equation 33 can be written as

$$\frac{V_p}{V_c} = \frac{v_r/\alpha_s v_s}{V_c \mu/v_s \sigma} \cdot \frac{2\Delta\tau_{p-r}}{\sigma}, \quad (34)$$

341 Equations 34 and 29 can predict well the relation among stress drop, peak slip rate, and rupture
342 speed for both SSEs and earthquakes (Figure 2).

A7. Critical stress drop and strength drop for steady ruptures Here I derive the critical stress drop for steady ruptures, $\Delta\tau^{steady}/\sigma$, under the framework of V-shape rate-and-state friction law, where G_0 and G_c can be written as (Methods A5)

$$\begin{aligned} G_0 &= \frac{\lambda W}{\mu} \Delta\tau^2, \\ G_c &= \frac{\lambda W}{\mu} \left[\frac{L_c}{2\lambda W} \Delta\tau_{p-r}^2 + \left(\frac{L_c}{2\lambda W} \Delta\tau_{p-r} + \Delta\tau \right) (\tau_r - \tau_f) \right]. \end{aligned} \quad (35)$$

For steady ruptures, the energy balance condition of equation 35 is

$$\left(\frac{\Delta\tau}{b\sigma} \right)^2 = \frac{L_c}{2\lambda W} \left(\frac{\Delta\tau_{p-r}}{b\sigma} \right)^2 + \left(\frac{L_c}{2\lambda W} \frac{\Delta\tau_{p-r}}{b\sigma} + \frac{\Delta\tau}{b\sigma} \right) \frac{\tau_r - \tau_f}{b\sigma}. \quad (36)$$

It is possible to analytically solve for $\Delta\tau^{steady}/b\sigma$ in equation 36, however the derivation of closed-form $\Delta\tau^{steady}/b\sigma$ is complex and lengthy and does not provide additional physical insight, therefore I numerically solve it. Considering $W/L_c \gg 1$, equation 36 can be simplified approximately as

$$\frac{\Delta\tau^{steady}}{b\sigma} = \frac{\tau_r - \tau_f}{b\sigma} = \frac{a}{b} \ln \left(\frac{aV_p}{3(b-a)V_c} \right) + \ln \left(\frac{\frac{3V_c}{V_p} + 1}{\frac{a}{b-a} + 1} \right). \quad (37)$$

343 Hawthorne and Rubin²³ noted that the critical stress drop for steady ruptures can be estimated
344 assuming $V_p/V_c \approx 15(b-a)/a$. Here, I use the approximate value of $V_p/V_c \approx 30(b-a)/a$ and
345 calculate $\Delta\tau^{steady}/b\sigma$ from equations 36 and 37. Both solutions can explain the simulation results

346 with an uncertainty of a factor of 2 (Figure S7). Given the values of $a/b = 0.8$, $b = 0.015$, and
 347 $W/L_c = 400$ used in this paper, the critical stress drop for steady ruptures is about $\Delta\tau^{steady}/\sigma \approx$
 348 0.01 , and substituting these values into equations 23 and 34 yields $v_r^{steady} \approx 50\alpha_s V_c \mu/\sigma$ and
 349 $\Delta\tau_{p-r}^{steady}/\sigma \approx 0.07$.

350 **A8. Moment-duration scaling relations of SSEs** I simulate single-rupture models by prescribing
 351 different values of initial shear stress to obtain moment-duration scaling relations of SSEs. The
 352 other model parameters are fixed and are the same as those described in Methods A3, except for a
 353 smaller $W/L_c = 100$ to reduce the computational cost and thus allow for a longer simulated fault,
 354 $20W$. For the homogeneous shear stress model, the stress drop is always lower than the steady
 355 stress drop, $\Delta\tau^{steady}$, which only results in self-arresting ruptures. For the linearly decaying shear
 356 stress model, the initial shear stress is largest near the nucleation zone and linearly decreases to
 357 zero at the other side of the fault. A minimum nucleation length, $0.1W$, with higher slip rates is
 358 prescribed to smoothly nucleate unilateral ruptures. For each rupture model, the rupture length,
 359 L , is determined by the end of the rupture tip, and the SSE duration, T , is estimated by a slip rate
 360 threshold, $0.1V_c$. Note that the SSE duration is slightly longer than the rupture time by a rise time.
 361 As the prescribed initial shear stress increases, the rupture length, L , moment, M_0 , and duration,
 362 T , of the SSEs increase accordingly. In the homogeneous shear stress model, L and M_0 increase
 363 toward infinity as stress drop asymptotically approaches $\Delta\tau^{steady}$.

For long ruptures, the moment is $M_0 \sim \Delta\tau W^2 L$, where L is the rupture length and $\Delta\tau$ and
 v_r are the average stress drop and rupture speed, respectively. The duration is $T \approx L/v_r$. The
 theory and numerical simulations predict two characteristic quantities for steady SSEs (Methods

A7): $\Delta\tau^{steady} \approx 0.01\sigma$ and $v_r^{steady} \approx 50V_c\mu/\sigma$, where σ is the effective normal stress, V_c is the critical slip rate, and μ is the shear modulus. Therefore, the moment and duration can be normalized as

$$\begin{aligned}\frac{M_0}{\Delta\tau^{steady}W^3} &\sim \frac{\Delta\tau}{\Delta\tau^{steady}} \cdot \frac{L}{W} \\ \frac{T}{W/v_r^{steady}} &\sim \frac{v_r^{steady}}{v_r} \cdot \frac{L}{W}.\end{aligned}\tag{38}$$

In the numerical simulations, L/W , $\Delta\tau/\Delta\tau^{steady}$, and v_r/v_r^{steady} are calculated. Defining $\Delta\tau/\Delta\tau^{steady} \propto (L/W)^\alpha$ and $v_r/v_r^{steady} \propto (L/W)^\beta$ leads to

$$\frac{M_0}{\Delta\tau^{steady}W^3} \sim \left(\frac{T}{W/v_r^{steady}} \right)^{\frac{1+\alpha}{1-\beta}}.\tag{39}$$

364 In the homogeneous shear stress model, if $\Delta\tau > \Delta\tau^{steady}$, ruptures steadily propagate
 365 through the entire fault with $\Delta\tau$ and v_r independent of rupture length L , that is $\alpha = 0$ and $\beta = 0$.
 366 If $\Delta\tau < \Delta\tau^{steady}$, self-arresting ruptures decelerate and gradually stop for various values of $\Delta\tau$,
 367 which roughly results in $\alpha = 0.25$ and $\beta = -0.25$ (Figure S3). Therefore, both steady and
 368 self-arresting ruptures in the homogeneous stress model produce a linear moment-duration scal-
 369 ing relation. However, in the linearly decaying shear stress model, the simulated models result in
 370 $\alpha = 0.5$ and $\beta = 0.5$ (Figure S3), which leads to a cubic scaling relation.

371 Because $\Delta\tau \propto \sigma$ and $v_r \propto 1/\sigma$ (equations 21, 34, and 23), the dimensional analysis of
 372 equation 38 shows that α and β are independent of σ , $M_0 \propto \Delta\tau^{steady} \propto \sigma$, and $T \propto \frac{1}{v_r^{steady}} \propto$
 373 σ , which is also validated by numerical simulations that are not shown here. Therefore, as σ
 374 systematically varies, the cubic scaling curve between M_0 and T moves diagonally in the $M_0 - T$
 375 space (Figure 4b).

376 In addition, similar dimensional analysis shows that M_0 is independent of V_c and $T \sim 1/V_c$.
377 As V_c systematically varies, the scaling curve moves vertically in the $M_0 - T$ space, that is
378 $T \propto 1/v_r \propto 1/V_c$, which can reconcile the separation between the cubic scaling of SSEs and
379 earthquakes.

- 380 1. Hirose, H., Hirahara, K., Kimata, F., Fujii, N. & Miyazaki, S. A slow thrust slip event fol-
382 lowing the two 1996 hyuganada earthquakes beneath the bungo channel, southwest japan.
383 *Geophysical Research Letters* **26**, 3237–3240 (1999).
- 384 2. Dragert, H., Wang, K. & James, T. S. A silent slip event on the deeper cascadia subduction
385 interface. *Science* **292**, 1525–1528 (2001).
- 386 3. Lowry, A. R., Larson, K. M., Kostoglodov, V. & Bilham, R. Transient fault slip in guerrero,
387 southern mexico. *Geophysical Research Letters* **28**, 3753–3756 (2001).
- 388 4. Ozawa, S., Murakami, M. & Tada, T. Time-dependent inversion study of the slow thrust event
389 in the nankai trough subduction zone, southwestern japan. *Journal of Geophysical Research:*
390 *Solid Earth* **106**, 787–802 (2001).
- 391 5. Ohta, Y., Freymueller, J. T., Hreinsdóttir, S. & Suito, H. A large slow slip event and the depth
392 of the seismogenic zone in the south central alaska subduction zone. *Earth and Planetary*
393 *Science Letters* **247**, 108–116 (2006).
- 394 6. Douglas, A., Beavan, J., Wallace, L. & Townend, J. Slow slip on the northern hikurangi
395 subduction interface, new zealand. *Geophysical Research Letters* **32** (2005).

- 396 7. Outerbridge, K. C. *et al.* A tremor and slip event on the cocos-caribbean subduction zone as
397 measured by a global positioning system (gps) and seismic network on the nicoya peninsula,
398 costa rica. *Journal of Geophysical Research: Solid Earth* **115** (2010).
- 399 8. Michel, S., Gualandi, A. & Avouac, J.-P. Interseismic coupling and slow slip events on the
400 cascadia megathrust. *Pure and Applied Geophysics* **176**, 3867–3891 (2019).
- 401 9. Rousset, B., Bürgmann, R. & Campillo, M. Slow slip events in the roots of the san andreas
402 fault. *Science advances* **5**, eaav3274 (2019).
- 403 10. Kato, A. *et al.* Propagation of slow slip leading up to the 2011 mw 9.0 tohoku-oki earthquake.
404 *Science* **335**, 705–708 (2012).
- 405 11. Ruiz, S. *et al.* Intense foreshocks and a slow slip event preceded the 2014 iquique mw 8.1
406 earthquake. *Science* **345**, 1165–1169 (2014).
- 407 12. Uchida, N., Iinuma, T., Nadeau, R. M., Bürgmann, R. & Hino, R. Periodic slow slip triggers
408 megathrust zone earthquakes in northeastern japan. *Science* **351**, 488–492 (2016).
- 409 13. Radiguet, M. *et al.* Triggering of the 2014 m w 7.3 papanao earthquake by a slow slip event
410 in guerrero, mexico. *Nature Geoscience* **9**, 829–833 (2016).
- 411 14. Michel, S., Gualandi, A. & Avouac, J.-P. Similar scaling laws for earthquakes and cascadia
412 slow-slip events. *Nature* **574**, 522–526 (2019).
- 413 15. Kano, M. *et al.* Development of a slow earthquake database. *Seismological Research Letters*
414 **89**, 1566–1575 (2018).

- 415 16. Fukao, Y. *et al.* Detection of “rapid” aseismic slip at the Izu-Bonin trench. *Journal of Geo-*
416 *physical Research: Solid Earth* **126**, e2021JB022132 (2021).
- 417 17. Kikuchi, M. & Kanamori, H. *Source characteristics of the 1992 Nicaragua tsunami earth-*
418 *quake inferred from teleseismic body waves*, 441–453 (Springer, 1995).
- 419 18. Ihmlé, P. F., Gomez, J.-M., Heinrich, P. & Guibourg, S. The 1996 Peru tsunamigenic earth-
420 quake: Broadband source process. *Geophysical Research Letters* **25**, 2691–2694 (1998).
- 421 19. Ammon, C. J., Kanamori, H., Lay, T. & Velasco, A. A. The 17 July 2006 Java tsunami earth-
422 quake. *Geophysical Research Letters* **33** (2006).
- 423 20. Mai, P. M. & Thingbaijam, K. Srcmod: An online database of finite-fault rupture models.
424 *Seismological Research Letters* **85**, 1348–1357 (2014).
- 425 21. Vallée, M., Charléty, J., Ferreira, A. M., Delouis, B. & Vergoz, J. Scardec: a new technique
426 for the rapid determination of seismic moment magnitude, focal mechanism and source time
427 functions for large earthquakes using body-wave deconvolution. *Geophysical Journal Inter-*
428 *national* **184**, 338–358 (2011).
- 429 22. Passelègue, F. X. *et al.* Initial effective stress controls the nature of earthquakes. *Nature*
430 *communications* **11**, 1–8 (2020).
- 431 23. Hawthorne, J. & Rubin, A. Laterally propagating slow slip events in a rate and state friction
432 model with a velocity-weakening to velocity-strengthening transition. *Journal of Geophysical*
433 *Research: Solid Earth* **118**, 3785–3808 (2013).

- 434 24. Shibazaki, B. & Iio, Y. On the physical mechanism of silent slip events along the deeper part
435 of the seismogenic zone. *Geophysical Research Letters* **30** (2003).
- 436 25. Shibazaki, B. & Shimamoto, T. Modelling of short-interval silent slip events in deeper subduc-
437 tion interfaces considering the frictional properties at the unstable—stable transition regime.
438 *Geophysical Journal International* **171**, 191–205 (2007).
- 439 26. Liu, Y. & Rubin, A. M. Role of fault gouge dilatancy on aseismic deformation transients.
440 *Journal of Geophysical Research: Solid Earth* **115** (2010).
- 441 27. Segall, P., Rubin, A. M., Bradley, A. M. & Rice, J. R. Dilatant strengthening as a mechanism
442 for slow slip events. *Journal of Geophysical Research: Solid Earth* **115** (2010).
- 443 28. Yamashita, T. & Suzuki, T. Dynamic modeling of slow slip coupled with tremor. *Journal of*
444 *Geophysical Research: Solid Earth* **116** (2011).
- 445 29. Brantut, N. Dilatancy toughening of shear cracks and implications for slow rupture propaga-
446 tion. *arXiv preprint arXiv:2104.06475* (2021).
- 447 30. Im, K., Saffer, D., Marone, C. & Avouac, J.-P. Slip-rate-dependent friction as a universal
448 mechanism for slow slip events. *Nature Geoscience* **13**, 705–710 (2020).
- 449 31. Ikari, M. J., Marone, C., Saffer, D. M. & Kopf, A. J. Slip weakening as a mechanism for slow
450 earthquakes. *Nature geoscience* **6**, 468–472 (2013).
- 451 32. Kaproth, B. M. & Marone, C. Slow earthquakes, preseismic velocity changes, and the origin
452 of slow frictional stick-slip. *Science* **341**, 1229–1232 (2013).

- 453 33. Leeman, J., Saffer, D., Scuderi, M. & Marone, C. Laboratory observations of slow earthquakes
454 and the spectrum of tectonic fault slip modes. *Nature communications* **7**, 1–6 (2016).
- 455 34. Weeks, J. D. Constitutive laws for high-velocity frictional sliding and their influence on stress
456 drop during unstable slip. *Journal of Geophysical Research: Solid Earth* **98**, 17637–17648
457 (1993).
- 458 35. Liao, Z., Chang, J. C. & Reches, Z. Fault strength evolution during high velocity friction ex-
459 periments with slip-pulse and constant-velocity loading. *Earth and Planetary Science Letters*
460 **406**, 93–101 (2014).
- 461 36. Buijze, L., Niemeijer, A. R., Han, R., Shimamoto, T. & Spiers, C. J. Friction properties and
462 deformation mechanisms of halite (-mica) gouges from low to high sliding velocities. *Earth*
463 *and Planetary Science Letters* **458**, 107–119 (2017).
- 464 37. Reches, Z. & Lockner, D. A. Fault weakening and earthquake instability by powder lubrication.
465 *Nature* **467**, 452–455 (2010).
- 466 38. Kilgore, B. D., Blanpied, M. L. & Dieterich, J. H. Velocity dependent friction of granite over
467 a wide range of conditions. *Geophysical Research Letters* **20**, 903–906 (1993).
- 468 39. Rabinowitz, H. *et al.* Frictional behavior of input sediments to the hikurangi trench, new
469 zealand. *Geochemistry, Geophysics, Geosystems* **19**, 2973–2990 (2018).
- 470 40. Shimamoto, T. Transition between frictional slip and ductile flow for halite shear zones at
471 room temperature. *Science* **231**, 711–714 (1986).

- 472 41. Weng, H. & Ampuero, J.-P. Continuum of earthquake rupture speeds enabled by oblique slip.
473 *Nature Geoscience* 1–5 (2020).
- 474 42. Bar Sinai, Y., Brener, E. A. & Bouchbinder, E. Slow rupture of frictional interfaces. *Geophys-*
475 *ical Research Letters* **39** (2012).
- 476 43. Ide, S., Beroza, G. C., Shelly, D. R. & Uchide, T. A scaling law for slow earthquakes. *Nature*
477 **447**, 76–79 (2007).
- 478 44. Gao, H., Schmidt, D. A. & Weldon, R. J. Scaling relationships of source parameters for slow
479 slip events. *Bulletin of the Seismological Society of America* **102**, 352–360 (2012).
- 480 45. Gomberg, J., Wech, A., Creager, K., Obara, K. & Agnew, D. Reconsidering earthquake scal-
481 ing. *Geophysical Research Letters* **43**, 6243–6251 (2016).
- 482 46. Frank, W. B. & Brodsky, E. E. Daily measurement of slow slip from low-frequency earth-
483 quakes is consistent with ordinary earthquake scaling. *Science advances* **5**, eaaw9386 (2019).
- 484 47. Takagi, R., Uchida, N. & Obara, K. Along-strike variation and migration of long-term slow
485 slip events in the western nankai subduction zone, japan. *Journal of Geophysical Research:*
486 *Solid Earth* **124**, 3853–3880 (2019).
- 487 48. Peng, Z. & Gomberg, J. An integrated perspective of the continuum between earthquakes and
488 slow-slip phenomena. *Nature geoscience* **3**, 599–607 (2010).

- 489 49. Thøgersen, K., Andersen Sveinsson, H., Scheibert, J., Renard, F. & Malthes-Sørensen, A.
490 The moment duration scaling relation for slow rupture arises from transient rupture speeds.
491 *Geophysical Research Letters* **46**, 12805–12814 (2019).
- 492 50. Dal Zilio, L., Lapusta, N. & Avouac, J. Unraveling scaling properties of slow-slip events.
493 *Geophysical Research Letters* **47**, e2020GL087477 (2020).
- 494 51. Weng, H. & Ampuero, J. The dynamics of elongated earthquake ruptures. *Journal of Geo-*
495 *physical Research: Solid Earth* (2019).
- 496 52. Weng, H. & Yang, H. Seismogenic width controls aspect ratios of earthquake ruptures. *Geo-*
497 *physical Research Letters* **44**, 2725–2732 (2017).
- 498 53. Garagash, D. I. Fracture mechanics of rate-and-state faults and fluid injection induced slip.
499 *Philosophical Transactions of the Royal Society A* **379**, 20200129 (2021).
- 500 54. Barenblatt, G. I., Barenblatt, G. I. & Isaakovich, B. G. *Scaling, self-similarity, and interme-*
501 *diat asymptotics: dimensional analysis and intermediate asymptotics* (Cambridge University
502 Press, 1996).
- 503 55. Perrin, G., Rice, J. R. & Zheng, G. Self-healing slip pulse on a frictional surface. *Journal of*
504 *the Mechanics and Physics of Solids* **43**, 1461–1495 (1995).
- 505 56. Rice, J. Heating and weakening of faults during earthquake slip. *Journal of Geophysical*
506 *Research: Solid Earth* **111** (2006).

- 507 57. Viesca, R. C. & Garagash, D. I. Ubiquitous weakening of faults due to thermal pressurization.
508 *Nature Geoscience* **8**, 875–879 (2015).
- 509 58. Gabriel, A., Ampuero, J., Dalguer, L. & Mai, P. M. Source properties of dynamic rupture
510 pulses with off-fault plasticity. *Journal of Geophysical Research: Solid Earth* **118**, 4117–
511 4126 (2013).
- 512 59. Segall, P. & Bradley, A. M. Slow-slip evolves into megathrust earthquakes in 2d numerical
513 simulations. *Geophysical Research Letters* **39** (2012).
- 514 60. Bletery, Q. & Nocquet, J.-M. Slip bursts during coalescence of slow slip events in cascadia.
515 *Nature Communications* **11**, 1–6 (2020).
- 516 61. Nocquet, J.-M. *et al.* Supercycle at the ecuadorian subduction zone revealed after the 2016
517 pedernales earthquake. *Nature Geoscience* **10**, 145–149 (2017).
- 518 62. Villegas-Lanza, J. C. *et al.* Active tectonics of peru: Heterogeneous interseismic coupling
519 along the nazca megathrust, rigid motion of the peruvian sliver, and subandean shortening
520 accommodation. *Journal of Geophysical Research: Solid Earth* **121**, 7371–7394 (2016).
- 521 63. Radiguet, M. *et al.* Slow slip events and strain accumulation in the guerrero gap, mexico.
522 *Journal of Geophysical Research: Solid Earth* **117** (2012).
- 523 64. Wallace, L. M. Slow slip events in new zealand. *Annual Review of Earth and Planetary*
524 *Sciences* **48**, 175–203 (2020).

- 525 65. Klein, E. *et al.* Deep transient slow slip detected by survey gps in the region of atacama, chile.
526 *Geophysical Research Letters* **45**, 12,263–12,273 (2018).
- 527 66. Liu, Y. Numerical simulations on megathrust rupture stabilized under strong dilatancy
528 strengthening in slow slip region. *Geophysical Research Letters* **40**, 1311–1316 (2013).
- 529 67. Brodsky, E. E. & Mori, J. Creep events slip less than ordinary earthquakes. *Geophysical*
530 *Research Letters* **34** (2007).
- 531 68. Obara, K., Hirose, H., Yamamizu, F. & Kasahara, K. Episodic slow slip events accompanied
532 by non-volcanic tremors in southwest japan subduction zone. *Geophysical Research Letters*
533 **31** (2004).
- 534 69. Di Toro, G. *et al.* Fault lubrication during earthquakes. *Nature* **471**, 494–498 (2011).
- 535 70. Allmann, B. P. & Shearer, P. M. Global variations of stress drop for moderate to large earth-
536 quakes. *Journal of Geophysical Research: Solid Earth* **114** (2009).
- 537 71. Zoback, M. D. *et al.* New evidence on the state of stress of the san andreas fault system.
538 *Science* 1105–1111 (1987).
- 539 72. Luo, Y., Ampuero, J.-P., Miyakoshi, K. & Irikura, K. *Surface rupture effects on earthquake*
540 *moment-area scaling relations*, 7–18 (Springer, 2018).
- 541 73. Thomas, A. M., Nadeau, R. M. & Bürgmann, R. Tremor-tide correlations and near-lithostatic
542 pore pressure on the deep san andreas fault. *Nature* **462**, 1048–1051 (2009).

- 543 74. Kanamori, H. Mechanism of tsunami earthquakes. *Physics of the earth and planetary interiors*
544 **6**, 346–359 (1972).
- 545 75. Sallarès, V. & Ranero, C. R. Upper-plate rigidity determines depth-varying rupture behaviour
546 of megathrust earthquakes. *Nature* **576**, 96–101 (2019).
- 547 76. Ma, S. A self-consistent mechanism for slow dynamic deformation and tsunami generation
548 for earthquakes in the shallow subduction zone. *Geophysical Research Letters* **39** (2012).
- 549 77. Corbi, F., Funicello, F., Brizzi, S., Lallemand, S. & Rosenau, M. Control of asperities size
550 and spacing on seismic behavior of subduction megathrusts. *Geophysical Research Letters* **44**,
551 8227–8235 (2017).
- 552 78. Dieterich, J. Applications of rate-and state-dependent friction to models of fault slip and
553 earthquake occurrence. *Treat. Geophys.* **4**, 107–129 (2007).
- 554 79. Kato, N. A possible model for large preseismic slip on a deeper extension of a seismic rupture
555 plane. *Earth and Planetary Science Letters* **216**, 17–25 (2003).
- 556 80. Dieterich, J. H. Modeling of rock friction: 1. experimental results and constitutive equations.
557 *Journal of Geophysical Research: Solid Earth* **84**, 2161–2168 (1979).
- 558 81. Luo, Y., Ampuero, J., Galvez, P., Van den Ende, M. & Idini, B. Qdyn: a quasi-dynamic
559 earthquake simulator (v1. 1). *Zenodo*.(doi: 10.5281/zenodo. 322459) (2017).
- 560 82. Ampuero, J.-P. Sem2dpack, a spectral element software for 2d seismic wave propagation and
561 earthquake source dynamics, v2.3.8. *Zenodo* (2012).

562 83. Noda, H. & Lapusta, N. Stable creeping fault segments can become destructive as a result of
563 dynamic weakening. *Nature* **493**, 518–521 (2013).

564 84. Freund, L. *Dynamic fracture mechanics* (Cambridge university press, 1998).

565 85. Rubin, A. & Ampuero, J. Earthquake nucleation on (aging) rate and state faults. *Journal of*
566 *Geophysical Research: Solid Earth* **110** (2005).

567 86. Ida, Y. The maximum acceleration of seismic ground motion. *Bulletin of the Seismological*
568 *Society of America* **63**, 959–968 (1973).

569 **Acknowledgements** This manuscript benefited from discussions with Jean-Paul Ampuero, M.P.A. van
570 den Ende, Quentin Bletery, and Jean-Mathieu Nocquet. I thank Jean-Paul Ampuero, Frédéric Cappa, and
571 Allan Rubin for their constructive comments in reviewing the early version of this manuscript. I am grateful
572 to Jean-Paul Ampuero for his suggestion of empirically estimating the average slip rate of the observed SSEs
573 and to analyze the recurrence time of earthquakes and moment-duration scaling resulting from the model.
574 This work was supported by the French government through the Investments in the Future project UCAJEDI
575 (ANR-15-IDEX-01) managed by the French National Research Agency (ANR).

576 **Correspondence** Correspondence should be addressed to Huihui Weng (email: weng@geoazur.unice.fr).

577 **Data availability** The numerical data used for the figures are presented in the Source data. The theoretical
578 data are presented in the Methods. Other data are previously published and available in the references
579 explained in the figure captions.

580 **Code availability** The open-source softwares SEM2DPACK and QDYN used in the fully dynamic and

581 quasi-dynamic rupture simulations are available at <https://github.com/jpampuero/sem2dpack>
582 and <https://github.com/ydluo/qdyn>.

583 **Competing Interests** The author declares that he has no competing interests.

584 **Figure 1 Sketch of slow and fast ruptures on subduction zone and their rupture**
585 **speeds.** (a) Sketch of subduction zone comprised of tsunamigenic, seismogenic, and
586 SSE zones with finite widths. Sketch shows rupture propagation of SSE (blue curves)
587 and earthquake (red curves) that start at the hypocenters indicated by red stars. (b) Sym-
588 bols represent estimates of rupture speed versus peak slip rate of observed SSEs^{14–16},
589 laboratory experiments²², tsunami earthquakes^{17–19} and regular earthquakes^{20,21} (error
590 bar indicates uncertainty when available; Methods A1). Dashed curves mark the theo-
591 retical predictions (Methods A6). $\Delta\tau_{p-r}$ and μ are the peak-to-residual strength drop at
592 the rupture front and shear modulus, respectively. (c) Models for G_c/G_0 integrating mul-
593 tiple frictional mechanisms. Purple curve represents one example of G_c/G_0 for SSEs.
594 Red dash and solid curves represent examples of G_c/G_0 for earthquakes. Gray arrows
595 indicate the evolution of rupture speed controlled by equation (1).

596 **Figure 2 Steady rupture speeds predicted by theory.** (a) Symbols represent steady
597 rupture speed as a function of stress drop based on fully dynamic (stars) and quasi-
598 dynamic (diamonds) simulations, with colour coded by critical slip rate (legend in (b)). v_s
599 and σ are the S-wave speed and effective normal stress, respectively. (b) Comparison
600 of rupture speeds between numerical simulations (stars and diamonds) and theoretical
601 prediction (black curve). (c) Comparison of peak slip rates between numerical simula-
602 tions and theoretical prediction. (d) Symbols represent observed $V_c\mu/\sigma v_s$ in laboratory
603 experiments^{34–40} (error bar indicates uncertainty), where $\mu = 40\text{GPa}$ and $v_s = 3330\text{m/s}$
604 are assumed. Gray region marks the possible gap of $V_c\mu/\sigma v_s$ in natural faults, whose

605 bottom boundary is approximated by the rupture speed of the observed "fastest" SSEs,
606 $v_r \sim 10m/s$.

607 **Figure 3 Non-steady ruptures due to along-strike heterogeneities.** (a) Curves show
608 the transition of rupture speeds from one steady state at segment 1 to another steady
609 state at segment 2 based on fully dynamic (coloured curves) and quasi-dynamic (grey
610 curves) simulations. The colour is coded by the steady rupture speed at segment 2. (b)
611 Rupture arresting distances inside a barrier versus the peak slip rate before reaching
612 the barrier, based on fully dynamic (coloured stars) and quasi-dynamic (grey diamonds)
613 simulations. The colour is coded by the steady rupture speed before reaching the barrier.
614 The inset shows the sketch of rupture propagation after reaching a barrier.

615 **Figure 4 Moment-duration scaling of SSEs controlled by heterogeneities.** (a) Lin-
616 ear and cubic moment-duration scaling relations based on models of homogeneous shear
617 stress (pink circles) and linear decaying shear stress (green triangles). $\Delta\tau^{steady}$ and v_r^{steady}
618 are the critical stress drop and rupture speed for steady SSEs. (b) The arrow shows that
619 the cubic scaling curve is diagonally shifted as effective normal stress σ decreases, pre-
620 dicted by the theory (Method A8). A linear envelope of moment-duration scaling (grey
621 region) is shown assuming a diverse values of σ .

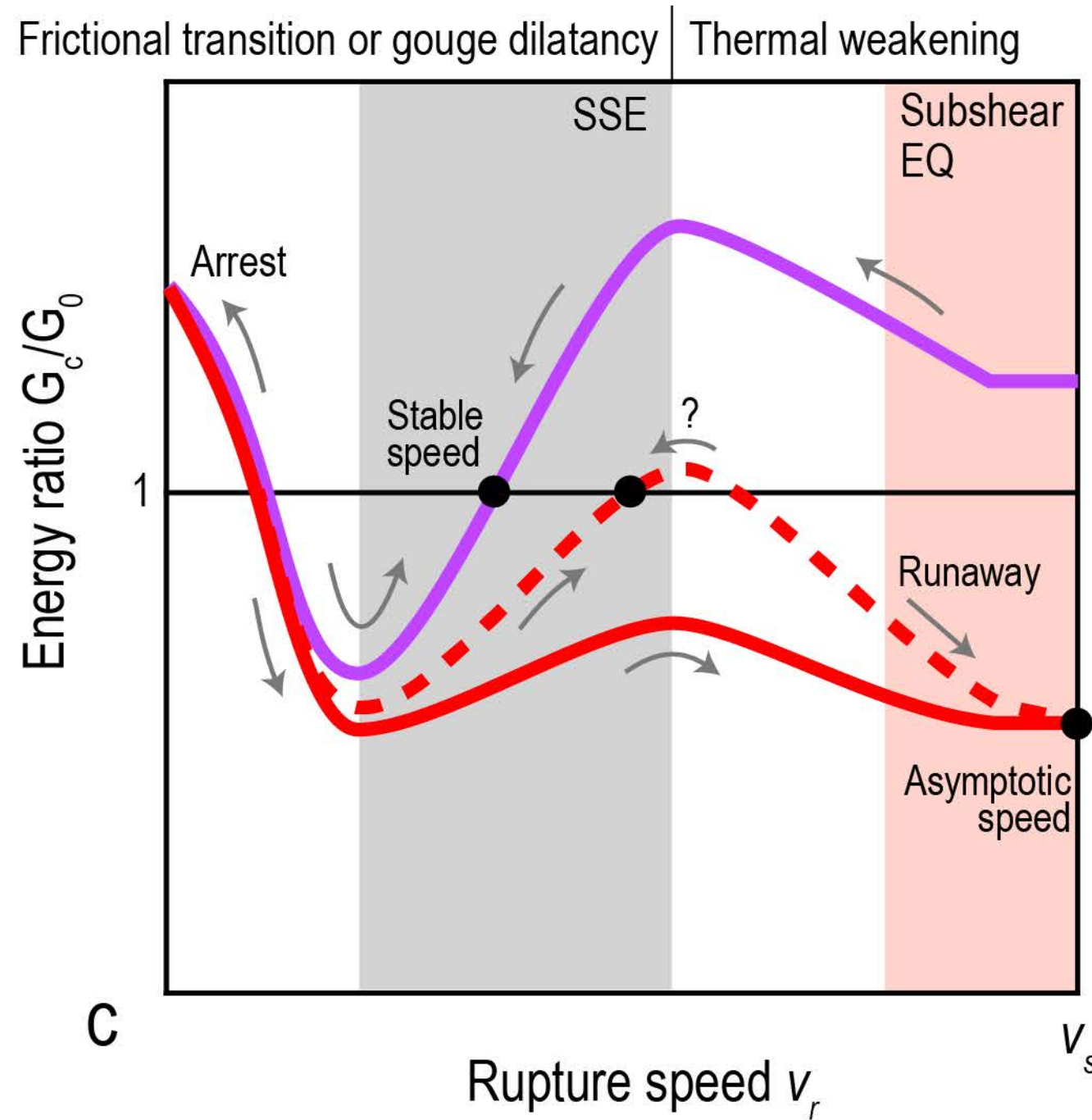
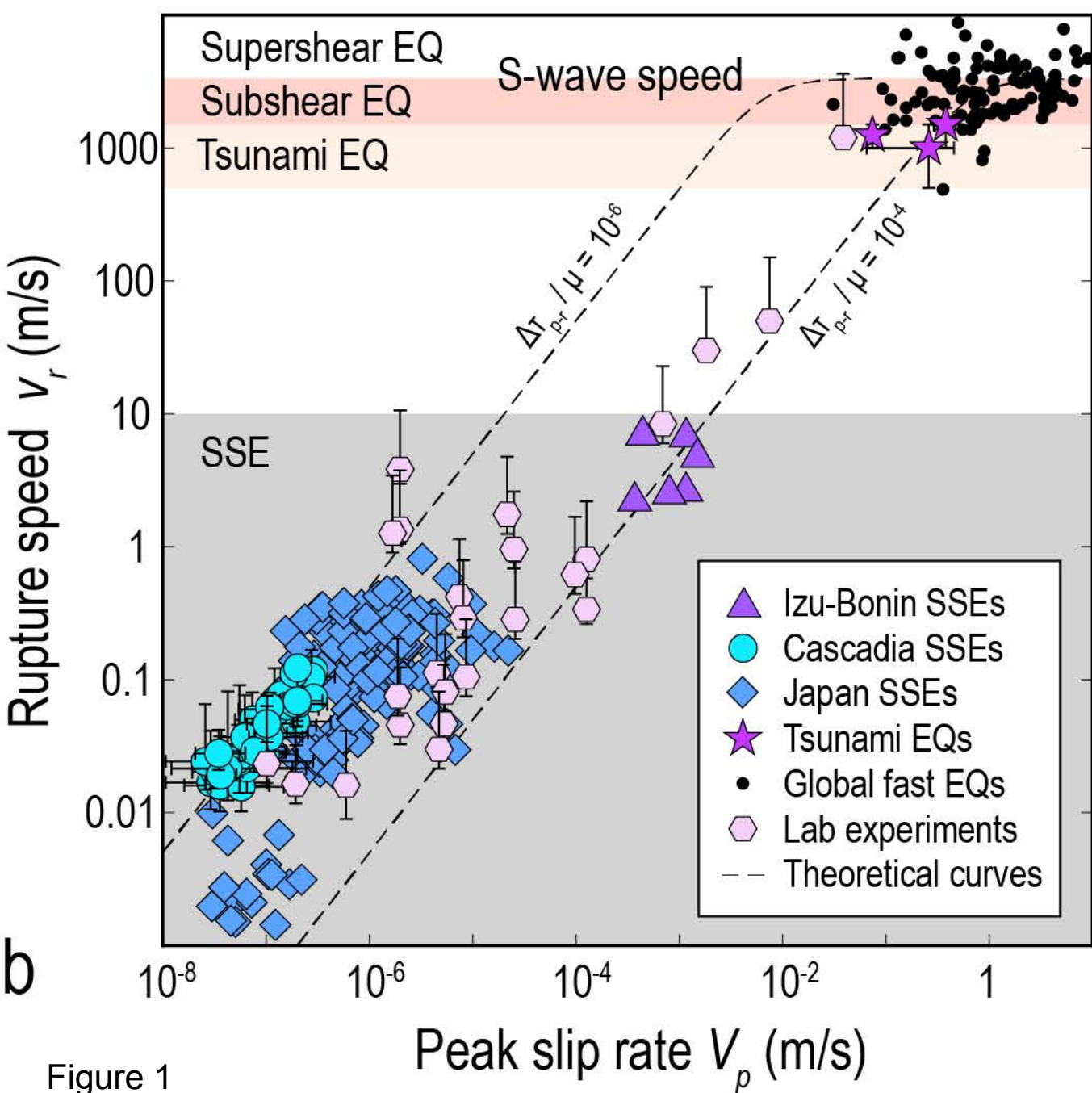
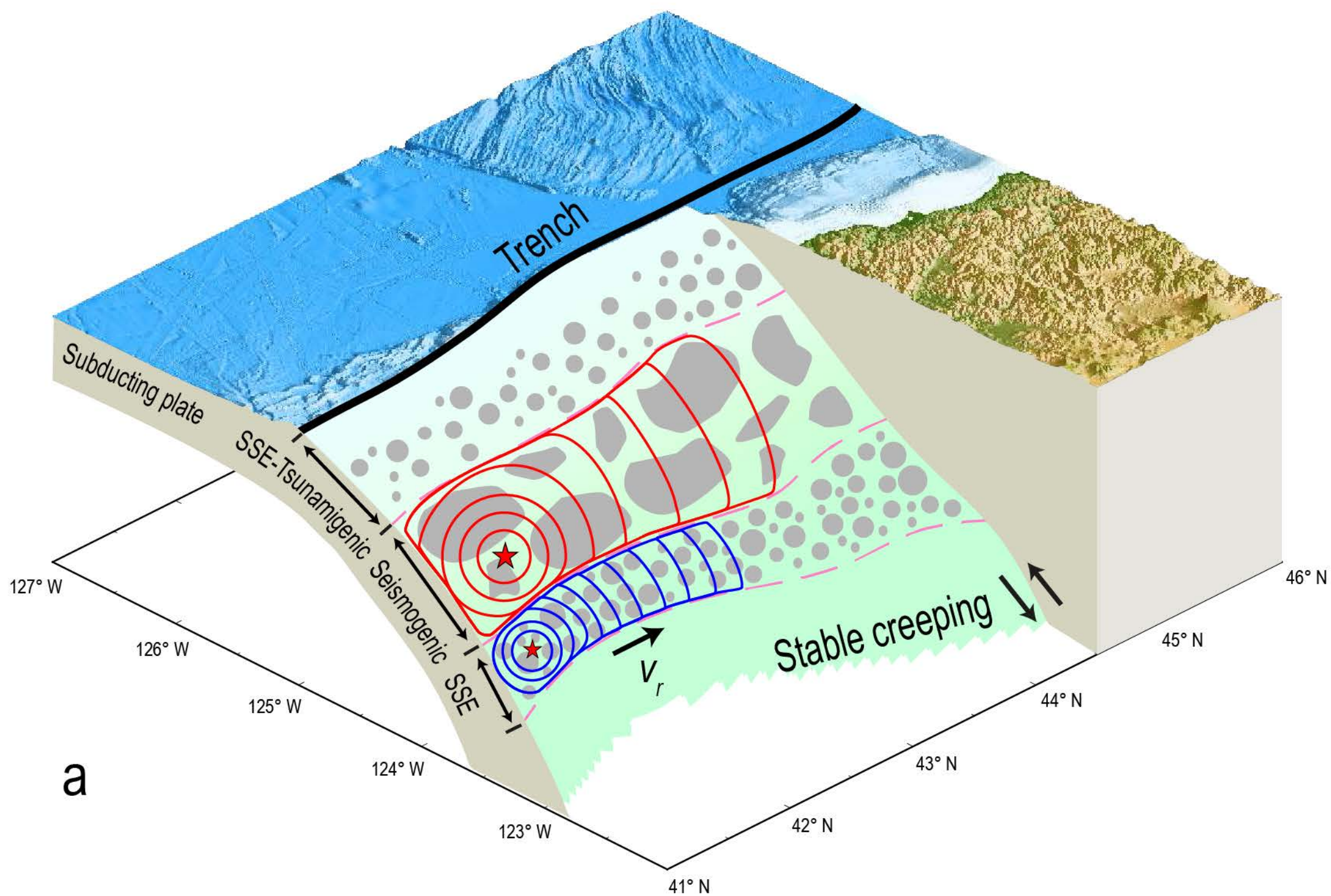


Figure 1

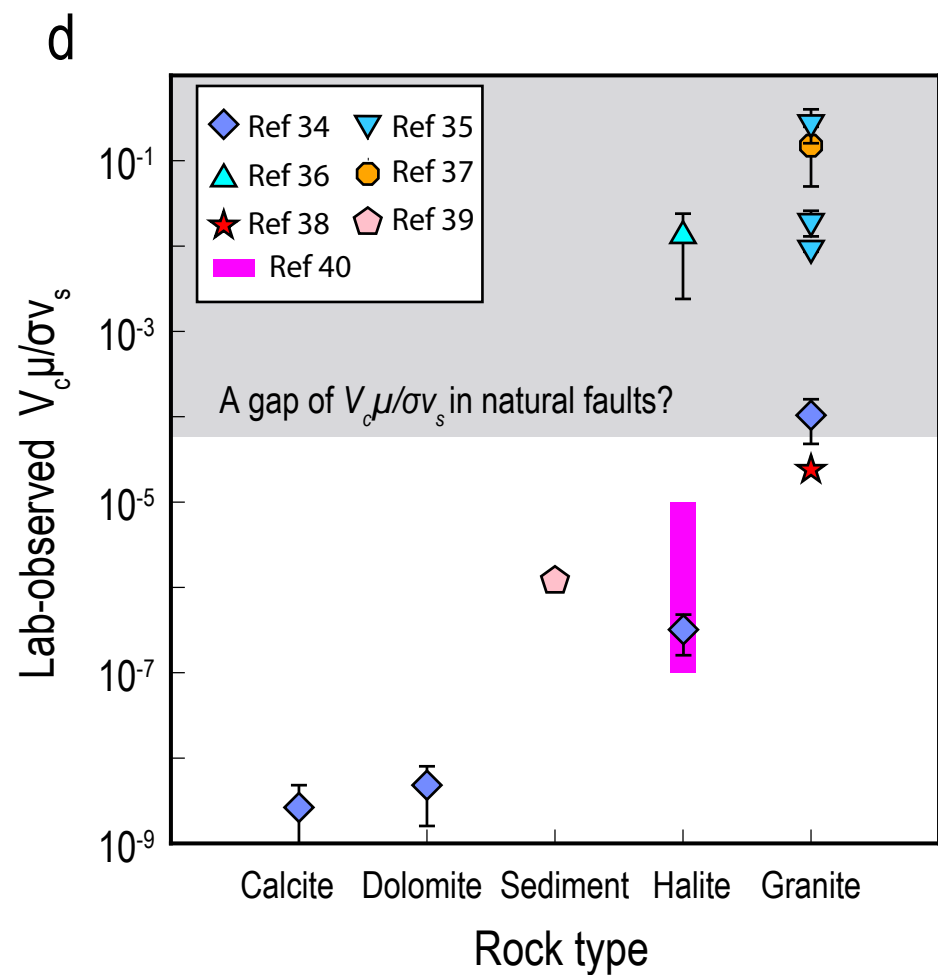
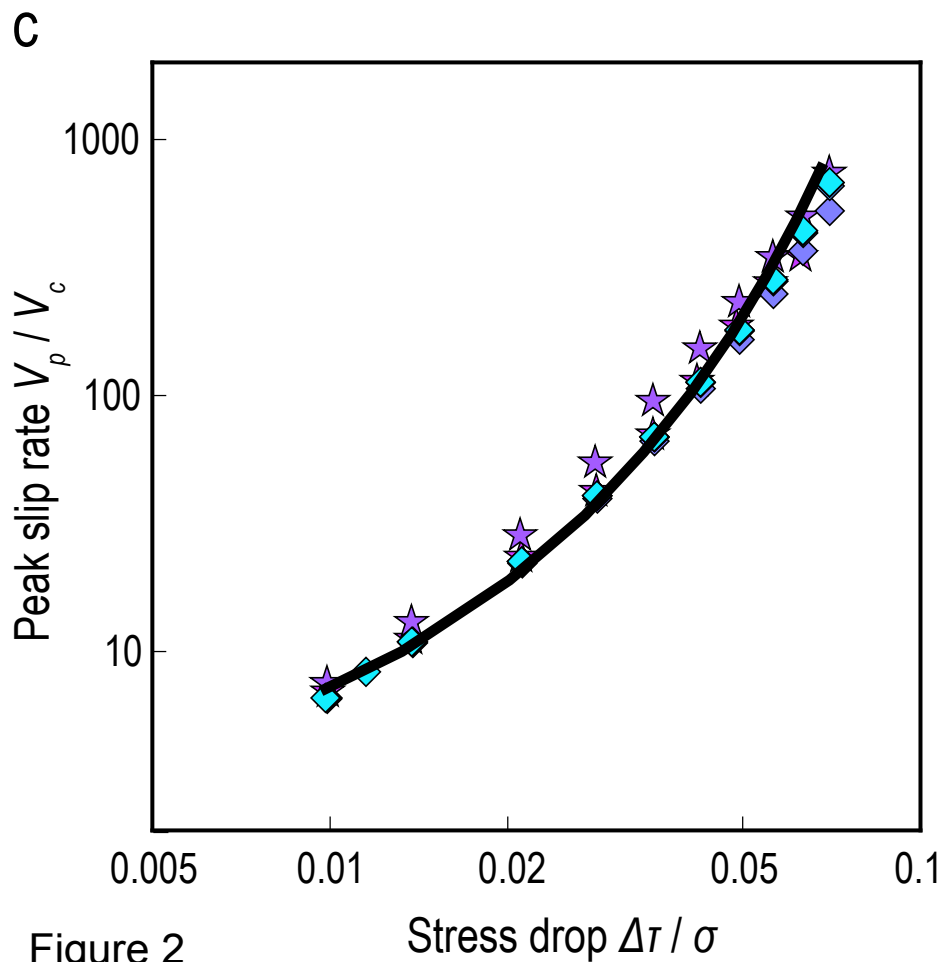
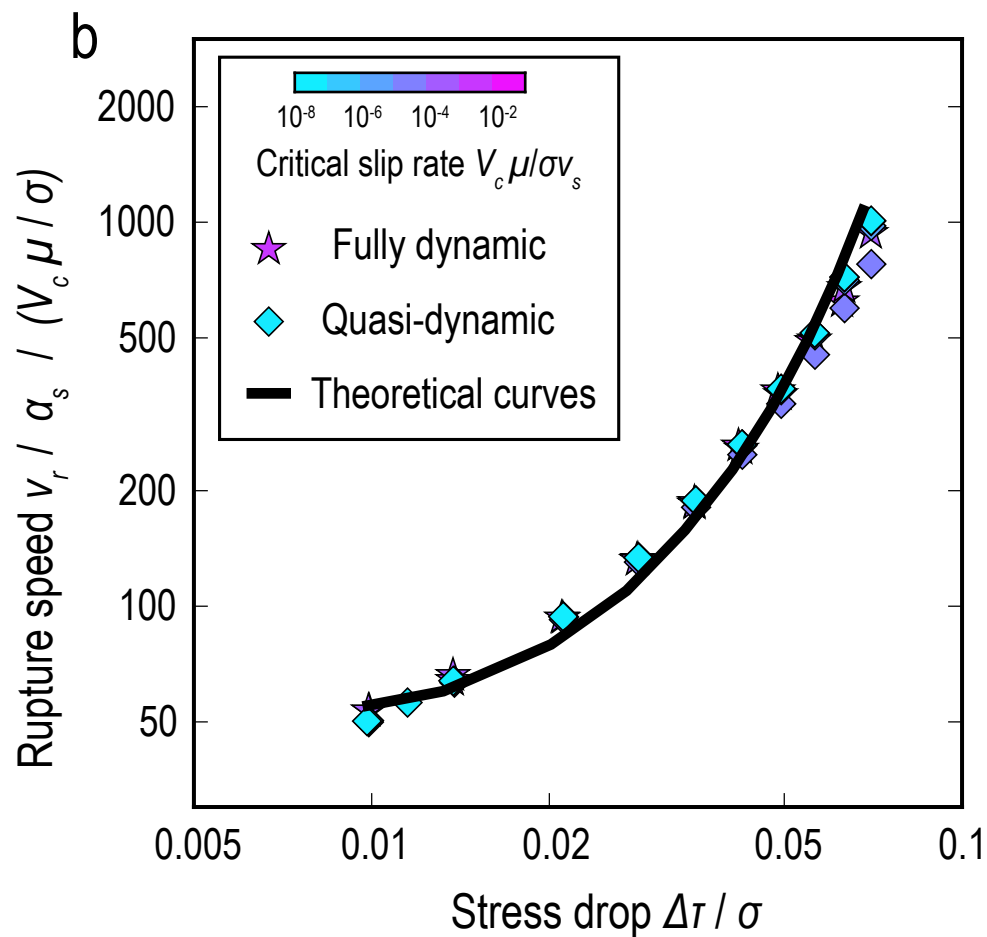
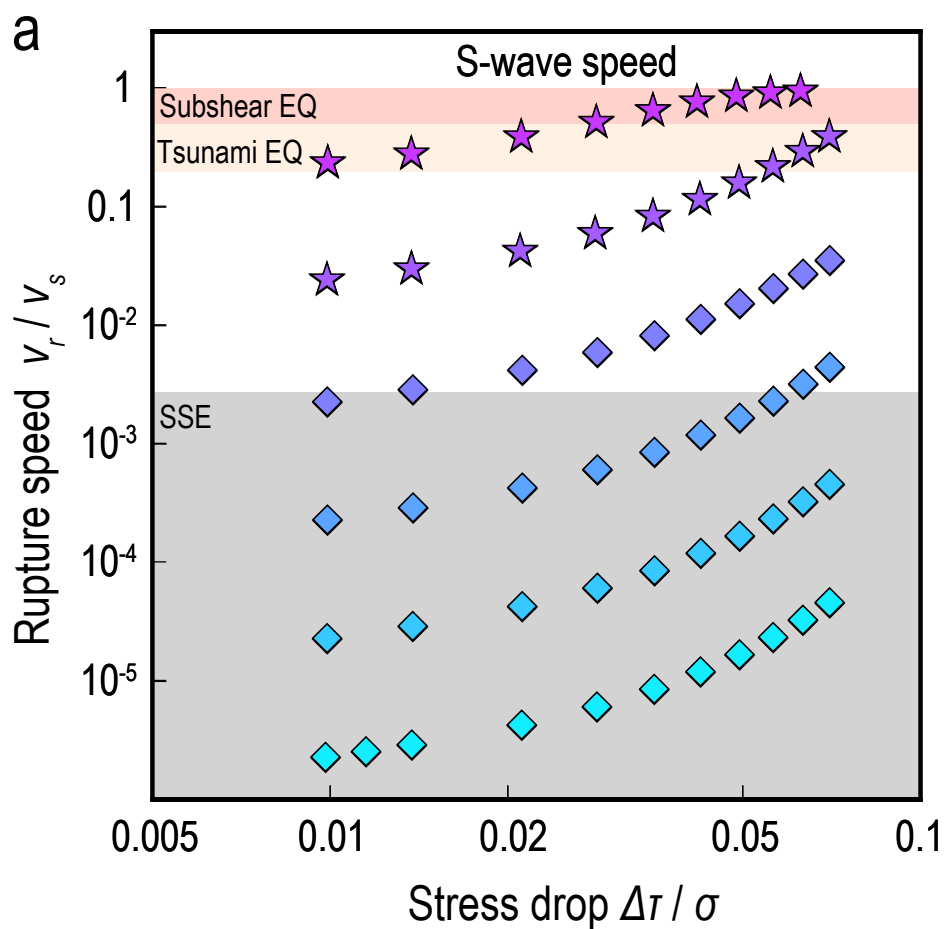


Figure 2

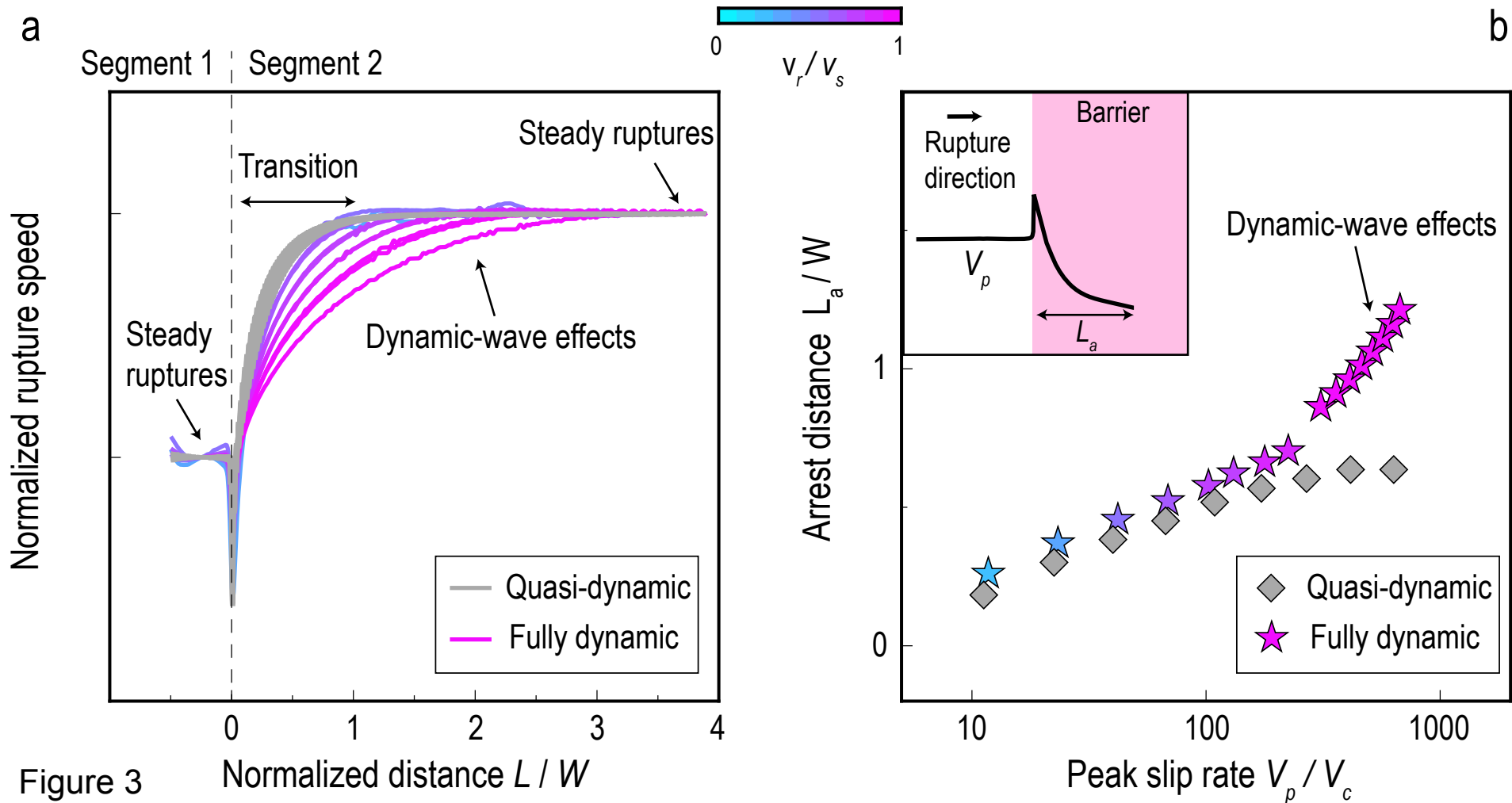


Figure 3

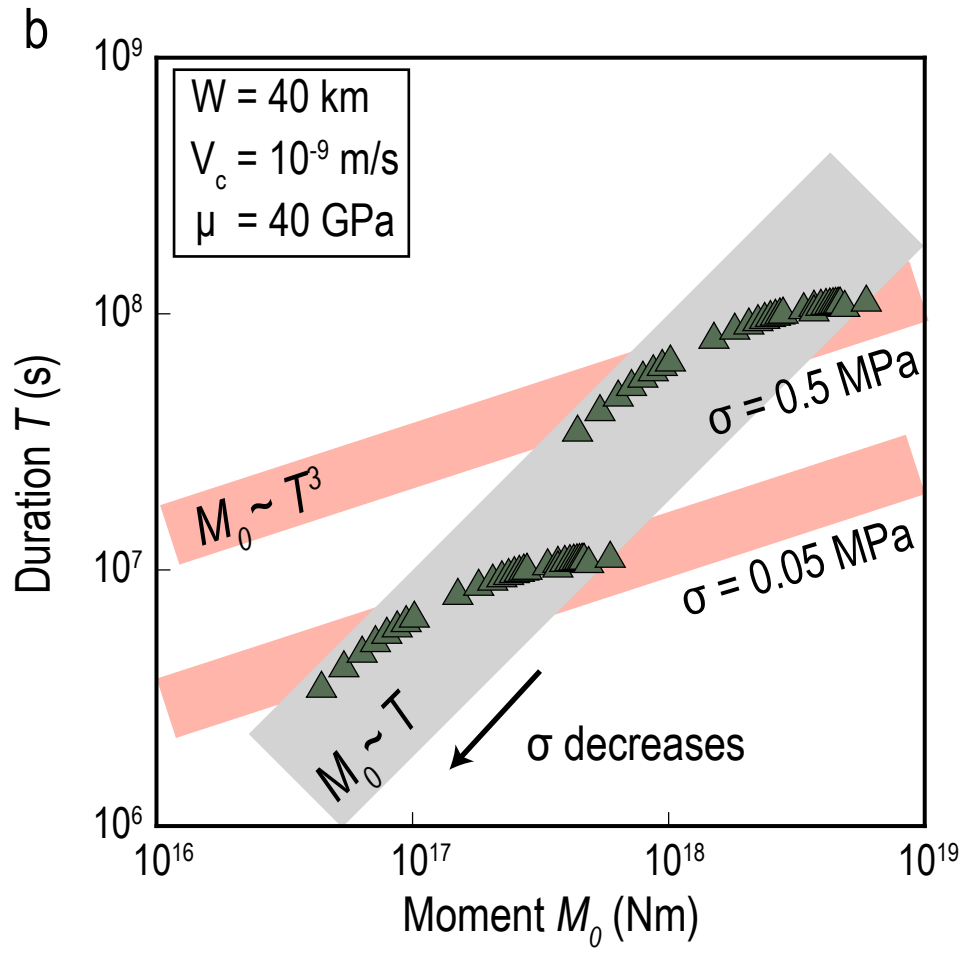
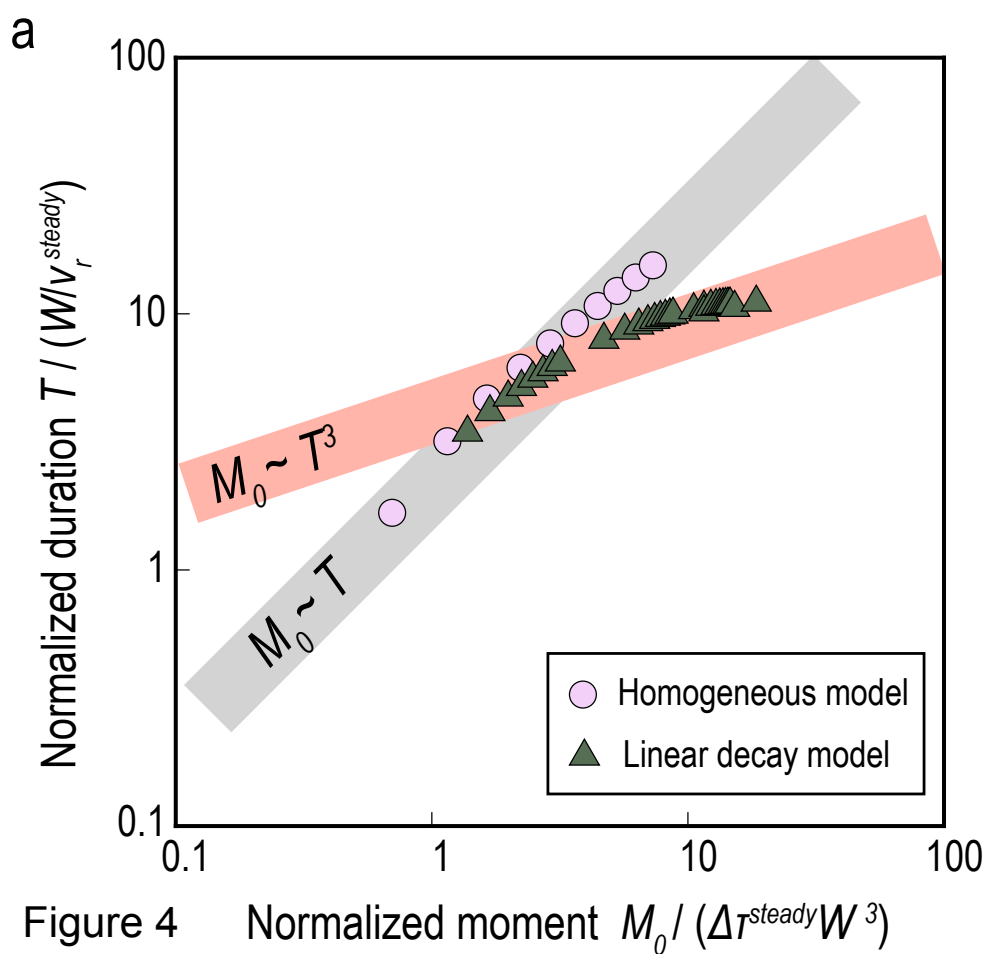


Figure 4 Normalized moment $M_0 / (\Delta\tau^{steady} W^3)$

Integrated rupture mechanics for slow slip events and earthquakes

Huihui Weng^{1*}

¹*Université Côte d'Azur, IRD, CNRS, Observatoire de la Côte d'Azur, Géoazur, 250 rue Albert Einstein, Sophia Antipolis, 06560 Valbonne, France*

Correspondence to Huihui Weng (email: weng@geoazur.unice.fr)

Contents

7 Supplementary Figures

Figure S1.

Figure S2.

Figure S3.

Figure S4.

Figure S5

Figure S6

Figure S7.

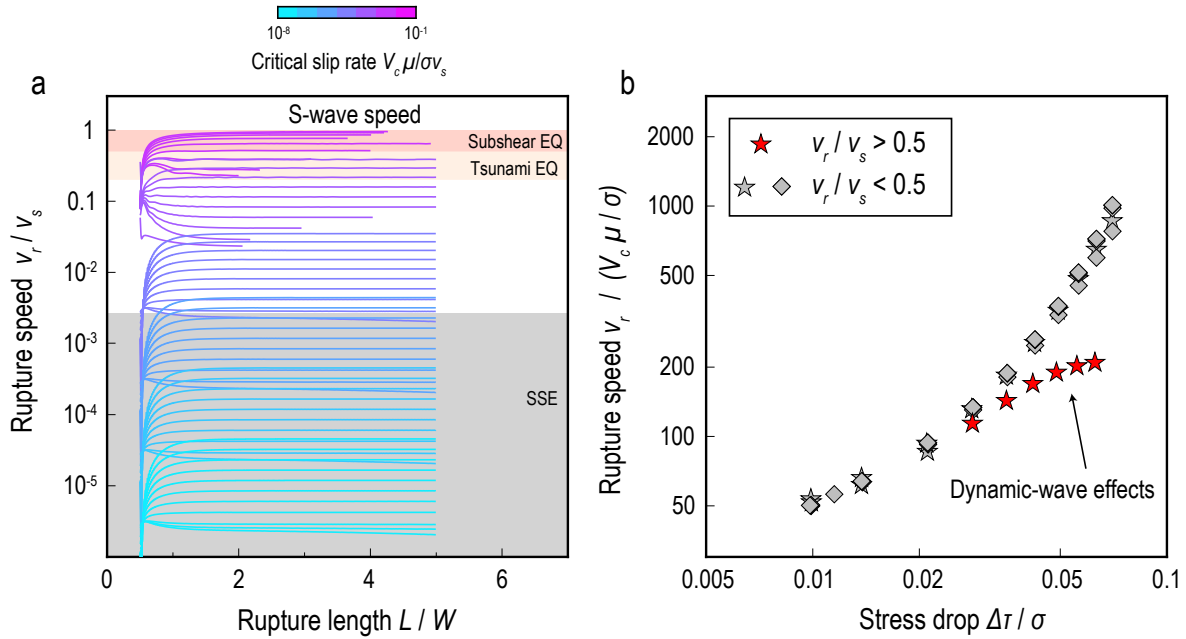


Figure S1: Rupture propagation of SSEs and earthquakes. (a) Coloured curves represent rupture speed as a function of normalized rupture distance based on fully dynamic and quasi-dynamic simulations (coloured curves coded by critical slip rate). (b) Normalized rupture speed (not accounting for the Lorentz contraction factor) versus normalized stress drop for simulated ruptures (legend).

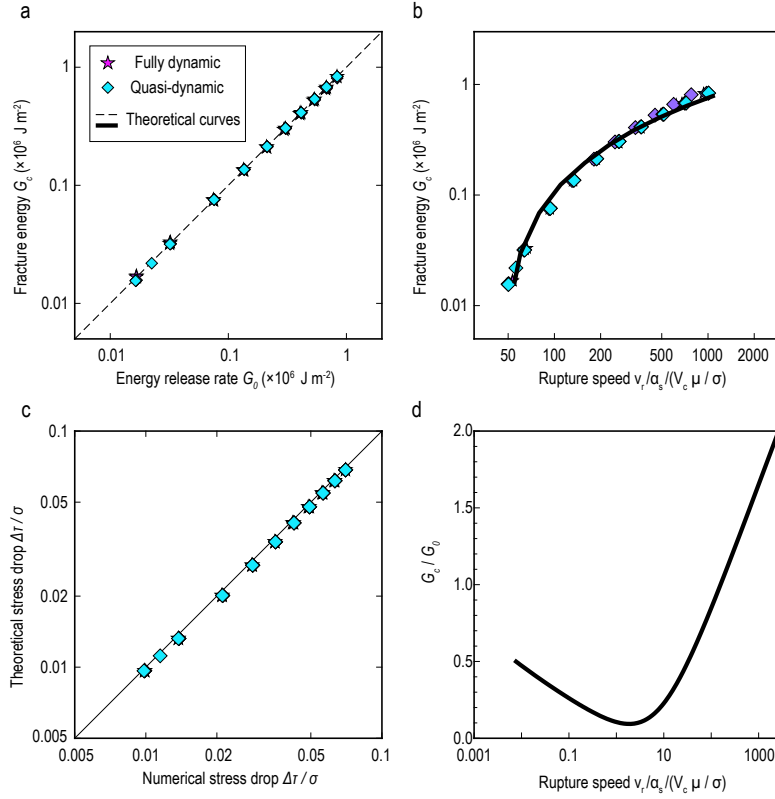


Figure S2: Energies of steady SSE and earthquake ruptures. (a) Symbols represent fracture energy and energy release rate numerically estimated from the fully dynamic and quasi-dynamic simulations (legend). The dashed line indicates the energy balance predicted by theory. (b) Fracture energy versus rupture speed based on simulations and theoretical prediction (black curve). (c) Comparison of stress drop between the numerical and theoretical estimates. (d) An example shows the dependency of G_c/G_0 on rupture speed v_r given an initial shear stress (Methods A5).

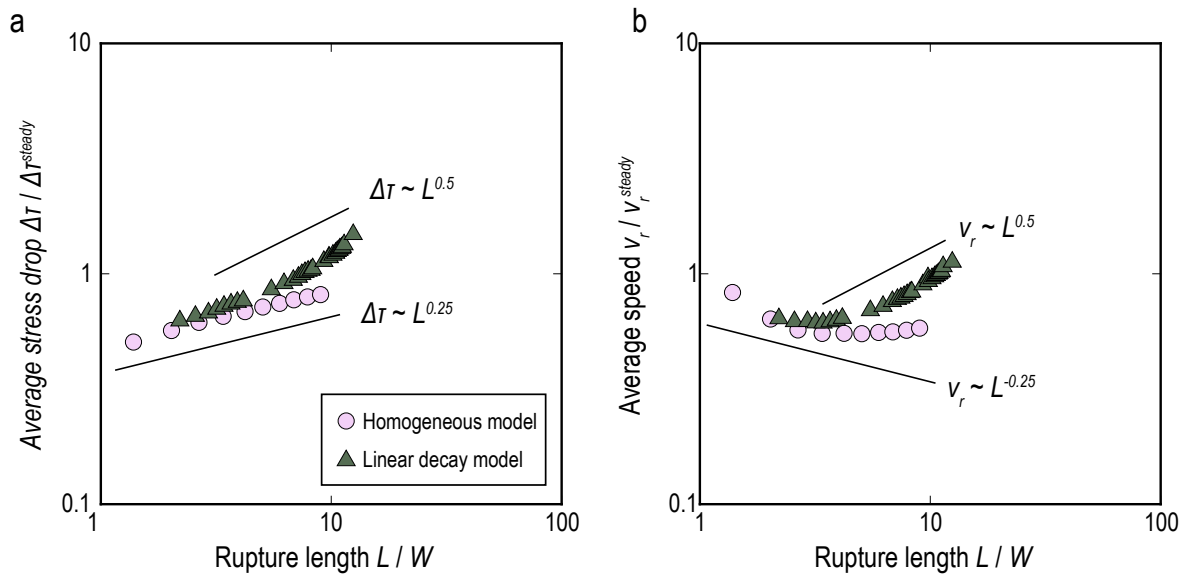


Figure S3: Scaling relations of stress drop and rupture speed. (a) Pink circles (homogeneous model) and green triangles (linear decay model) represent the scaling relation between stress drop and rupture length. (b) The scaling relation between rupture speed and rupture length.

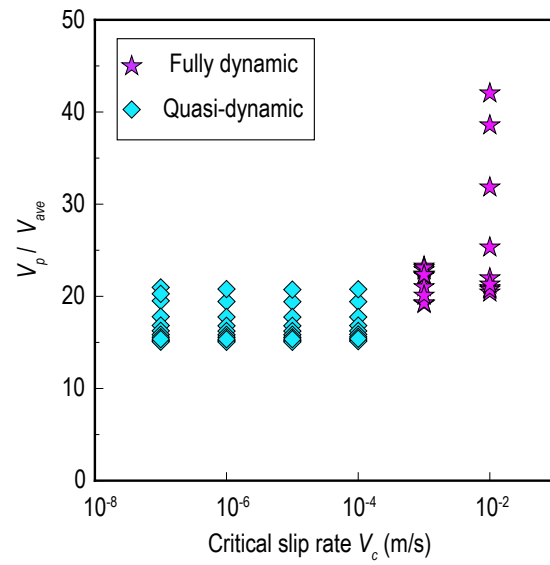


Figure S4: Empirical ratio between peak and average slip rates. Symbols represent the ratio of peak slip rate to average slip rate for various critical slip rates based on fully dynamic (stars) and quasi-dynamic (diamonds) simulations.

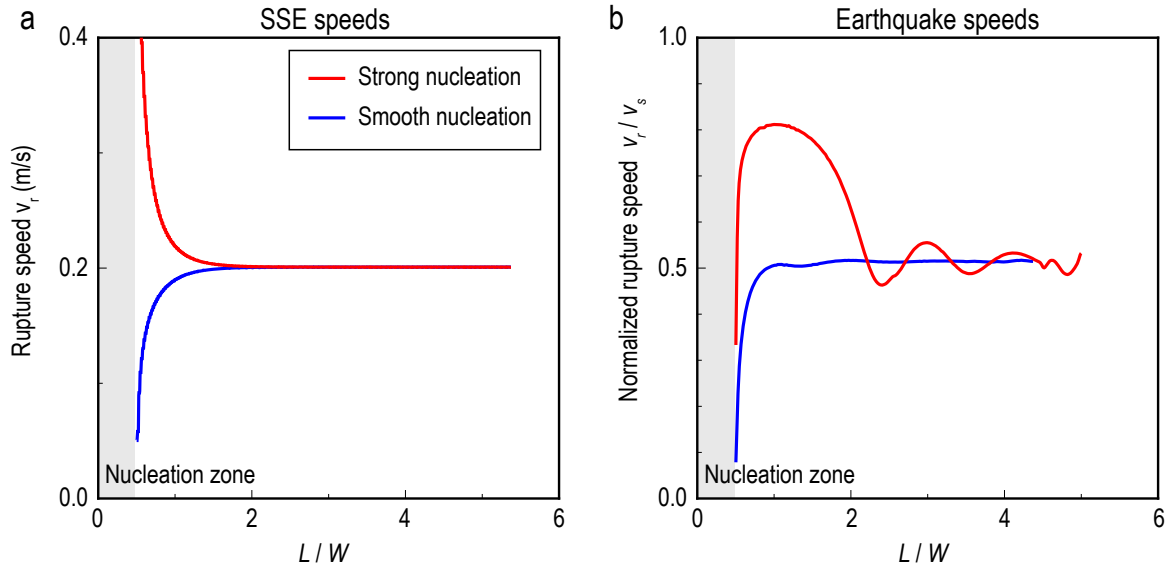


Figure S5: Effects of nucleation conditions on steady rupture propagation. (a) Rupture speeds as a function of normalized distance for two quasi-dynamic SSE simulations with different nucleation strategies: strong overstressed nucleation and smooth nucleation. The grey region marks the nucleation zone. (b) same as (a), but for fully dynamic earthquake simulations.

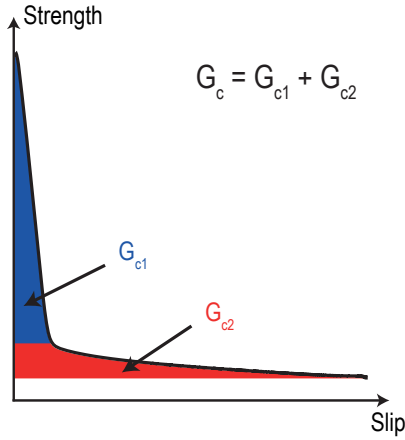


Figure S6: One example of fault strength evolution The evolution of fault strength as a function of fault slip governed by V-shape rate-and-state friction. The blue region marks the fracture energy caused by the first weakening stage. The red region marks the fracture energy caused by the second weakening stage.

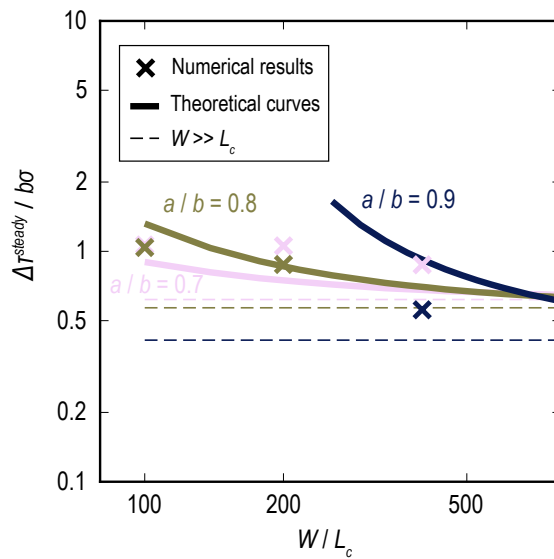


Figure S7: Dependence of critical stress drop for runaway ruptures The critical stress drop $\Delta\tau_{run}/b\sigma$ versus W/L_c for different values of a/b (colours), based on the numerical simulations (cross symbols) and the theoretical predictions (thick and dash curves).